Title

Simulations of carbon dioxide push-pull into a conjugate fault system modeled after Dixie Valley-Sensitivity analysis of significant parameters and uncertainty prediction by data-worth analysis

Authors

Lee, Kyung Jae
Oldenburg, Curtis M
Doughty, Christine
et al.

Publication Date

2018-07-01

DOI

10.1016/j.geothermics.2018.02.011

Peer reviewed

Simulations of carbon dioxide push-pull into a conjugate fault system modeled after Dixie Valley—Sensitivity analysis of significant parameters and uncertainty prediction by data-worth analysis

Author links open overlay panelKyung JaeLee[a]Curtis M.Oldenburg[a]ChristineDoughty[a]YoojinJung[a]AndreaBorgia[a]LehuaPan[a]RuiZhang[b]Thomas M.Daley[a]BilginAltundas[c]NikitaChugunov[c]
Show more

https://doi.org/10.1016/j.geothermics.2018.02.011Get rights and content

Highlights

- We investigate CO_2 push-pull into faults zones at Enhanced Geothermal Systems for improved characterization of major flow features.
- We developed a conceptual and numerical reservoir model of two intersecting faults based on the Dixie Valley geothermal system in Nevada, USA.
- We perform forward modeling along with sensitivity and data-worth analyses of $scCO_2$ push-pull to investigate the CO_2distribution in the faults.
- Formal sensitivity analysis determines the most controlling unknown parameters in the fault zones.
- Data-worth analysis reveals the most valuable output response to be measured for the best prediction of CO_2 distribution in the faults.

Abstract

Characterizing the faults and fractures that provide flow pathways for efficient geothermal energy production is critical for design of sustainable geothermal energy production. Both natural faults and stimulated fractures in enhanced geothermal systems (EGS) are difficult to image and map by seismic methods because hot brine filling the fractures and faults does not create a strong seismic property contrast relative to surrounding rock. We investigate here the technical feasibility of using supercritical CO_2 ($scCO_2$) injection into faults in a single-well push-pull scenario to characterize the

hydraulic properties of the fault zone by emplacing $scCO_2$ that can serve as a contrast fluid for seismic monitoring. We develop a conceptual and numerical reservoir model of two intersecting faults based on the Dixie Valley geothermal system in Nevada, USA. The 2D conceptual model consists of a system with a main fault and an intersecting conjugate fault. The corresponding numerical model is discretized using irregular grid blocks with fine discretization around the slip plane, gouge, and damage zones. We perform forward modeling along with sensitivity and data-worth analyses of $scCO_2$ push-pull to investigate the CO_2 distribution in the fault gouge during 30 days of push (injection) and 30 days of pull (production). Formal sensitivity analysis is conducted to determine the most controlling unknown parameters in the fault zones. Using the selected set of unknown parameters and output responses, we perform data-worth analysis to reveal the most valuable output response to be measured for the best prediction of CO_2 distribution in the fault zones and its uncertainty. From the results of data-worth analysis, we determine the optimal properties to target in monitoring, their locations, and the minimum observation time. Our results provide information on the optimal design of $scCO_2$ push-pull testing in a conjugate fault system modeled after Dixie Valley that can be used to enhance monitoring by active seismic and well-logging methods to better characterize the transmissive fault(s).

- **Previous** article
- **Next** article

Keywords

Enhanced geothermal sites (EGS)
CO_2 push-pull
Dixie Valley geothermal system
Sensitivity analysis
Data-worth analysis

1. Introduction

Networks of naturally occurring and engineered fractures and faults must be explored and characterized in order to optimize exploitation of geothermal energy from enhanced geothermal sites (EGS). However, faults and fractures occurring in many EGS sites are difficult to image with traditional seismic and well-logging tools because they are filled with hot brine and not easily distinguishable from the surrounding formation. Previous research showed that the injection (push) of supercritical CO_2 ($scCO_2$) into (i) a fracture zone at a geologic carbon sequestration site with active source seismic

monitoring (e.g., Zhang et al., 2015) and (ii) into a fault zone at a prototypical EGS site with active-source seismic monitoring and well-logging allowed seismic detection of the transmissive zones (Borgia et al., 2017; Oldenburg et al., 2016). After imaging the fracture and fault zone following injection, fluid production (pull) from the fault zone allows partial recovery of the injected $scCO_2$.

There are several advantages to using $scCO_2$: (1) much higher compressibility of $scCO_2$ relative to water facilitates seismic detection by changing the stiffness tensor components; (2) the non-wetting characteristic of $scCO_2$tends to exclude the $scCO_2$ from the matrix leaving it preferentially within the fractures and faults; (3) the smaller viscosity of $scCO_2$ relative to brine helps it to easily permeate into the fractures and faults; and (4) the higher density of $scCO_2$ relative to other gases mitigates the buoyancy effect and enables the better recovery of injected CO_2 during the pull phase (Borgia et al., 2017).

In this study, we investigate the technical feasibility of a $scCO_2$ push-pull test in the conjugate faults system of the geothermal resource at Dixie Valley in central Nevada, USA. The geothermal system in the Dixie Valley is of basin-and-range type, and the temperature of the field is estimated to approach a 260 °C at a depth of 3 km, based on measured well data (Blackwell et al., 2007; Iovenitti et al., 2016). The geothermal system in the Dixie Valley is believed to be a promising EGS site owing to high temperature range at relatively shallow depth, existence of faults and brittle fractured zones for permeability, and favorable stress regime at the depth of 1–3 km for EGS development (Iovenitti et al., 2016).

In the forward modeling of $scCO_2$ push-pull in this study, we simulate the injection and production of $scCO_2$ into the junction of two conjugate faults in the Dixie Valley Geothermal System (DVGS). We investigate the efficacy of injecting and producing CO_2 so that it spreads in the fault zones where it can be useful for improving imaging and characterization by seismic methods.

We conduct a sensitivity analysis to evaluate the factors affecting CO_2 inflow into the faults and outflow from the faults. The sensitivity coefficient of each influential parameter on the system response is quantified. We conduct a data-worth analysis to predict the uncertainty of CO_2 distribution after the push and pull phases by measuring the system responses. In this procedure, the data worth of each measurement is computed to indicate the relative importance for the prediction of future system behavior.

From this study, we determine (1) technical feasibility of CO_2 push-pull in the DVGS fault zones, (2) important flowing parameters in fault zones that affect the efficiency of CO_2 push-pull in the Dixie Valley geothermal system, (3) system responses that should

be measured to predict CO_2distribution after push-pull, and (4) prediction uncertainty of CO_2 distribution in the conjugate faults.

2. Dixie Valley geothermal system

The DVGS is one of the most thoroughly characterized geothermal systems in the U.S. The data include geological cross-sections, gravity-magnetic surveys, lithologic and resistivity models, seismic models of P-wave velocity and S-wave velocity, and thermal numerical models (Blackwell et al., 2009; Iovenitti et al., 2016; Iovenitti et al., 2013; Smith et al., 2011).

The DVGS occupies an area of approximately 170 km^2within the larger project area of 2500 km^2 (Iovenitti et al., 2016). In the geothermal system, there are a number of N-to NE-trending fault systems identified from thermal anomalies (Fig. 1(a)), which are formed by well-connected normal and associated conjugate faults of 1–3 km-depth.

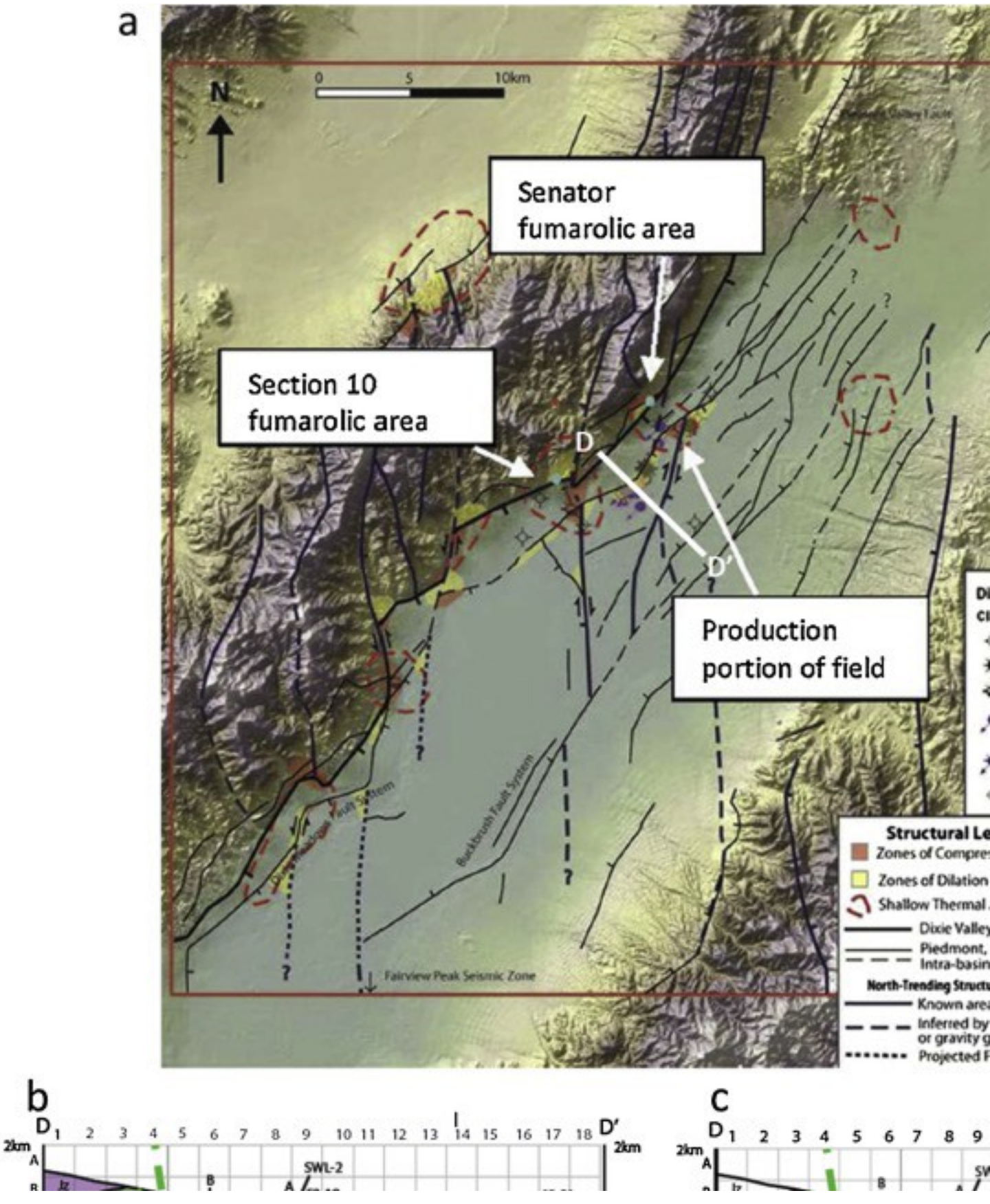
a
N
0
5
10km
Senator
fumarolic area
Section 10
fumarolic area
D
D'
Production
portion of field
Buckbrush Fault System
Fairview Peak Seismic Zone
Structural Le
Zones of Compres
Zones of Dilation
Shallow Thermal
Dixie Valley
Piedmont,
Intra-basin
North-Trending Structu
Known area
Inferred by
or gravity g
Projected F
b
D
D'
2km
A
B
SWL-2
c
D
2km
A
B

1. Download high-res image (2MB)
2. Download full-size image

Fig. 1. The Dixie Valley Geothermal System as depicted by (Iovenitti et al., 2016): (a) structural intersections of faults (dark blue lines) identified by thermal anomalies (dashed red lines) in the geothermal field, (b) geologic cross section following DD', (c) isotherms along the profile DD'. The blue outline box superimposed on the cross-sections of Iovenitti et al. (2016)shows our model domain boundary. (For interpretation of the references to colour in this figure legend, the reader is referred to the web version of this article.)

The geologic cross section DD' is shown in Fig. 1(b). Here, brittle and permeable zones within the Tbf (basin-filling sediments), Tmb (Miocene basalt), Jz (Jurassic mafic volcanics), and Tr (Triassic meta-sediments) provide the flow pathways of fluid and heat.

Hot brine rises along the main faults giving rise to the isotherms shown in Fig. 1(C) (Smith et al., 2011). Regarding the system temperature, depth, and the distributions of high-permeability zones, we define our model domain area of 2750 m × 2750 m as shown in Fig. 2.

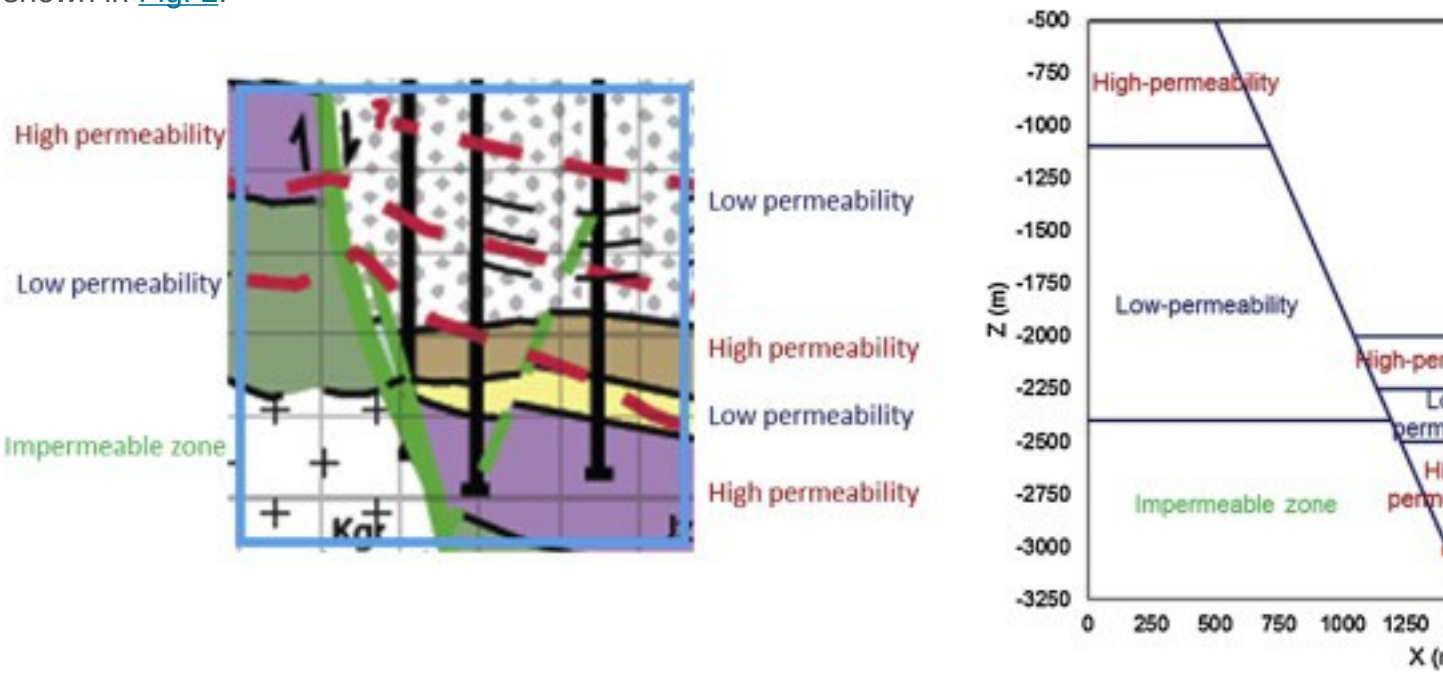

1. Download high-res image (327KB)
2. Download full-size image

Fig. 2. Lithology structure and size of the 2D model domain based on the DVGS.

3. Development of the conceptual and numerical models

We developed a 2D cross-sectional conceptual model of the DVGS involving the main and conjugate faults. The conceptual model includes the geometry of reservoir rocksand faults, as well as simplified representation of system heterogeneity, initial conditions, and transport properties. Although the conceptual model is very simplified, it includes the essential components that affect flow of injected $CO_2$and therefore retains the fundamental fault-flow-related aspects of the system. We chose to use a 2D model over a 3D model for computational efficiency. This choice is justified by the observation that a CO_2 plume in a steeply dipping fault zone expands more easily upward than horizontally due to buoyancy as observed in a3D simulation study (Borgia et al., 2017).
Fig. 3(a) shows the grid we developed for the 2D domain using WinGridder (Pan, 2008) corresponding to the cross section DD' (Fig. 1(a)). The model contains a total of 10,728 grid blocks. This irregular grids system has elements connected along the fault zones parallel to flow directions, rather than staggered connections that result from regular rectangular grids system. The expanded view at the junction of the faults is shown in Fig. 3(b). The width and height of the elements in the fault zones are 2.5 m and 10 m, respectively.

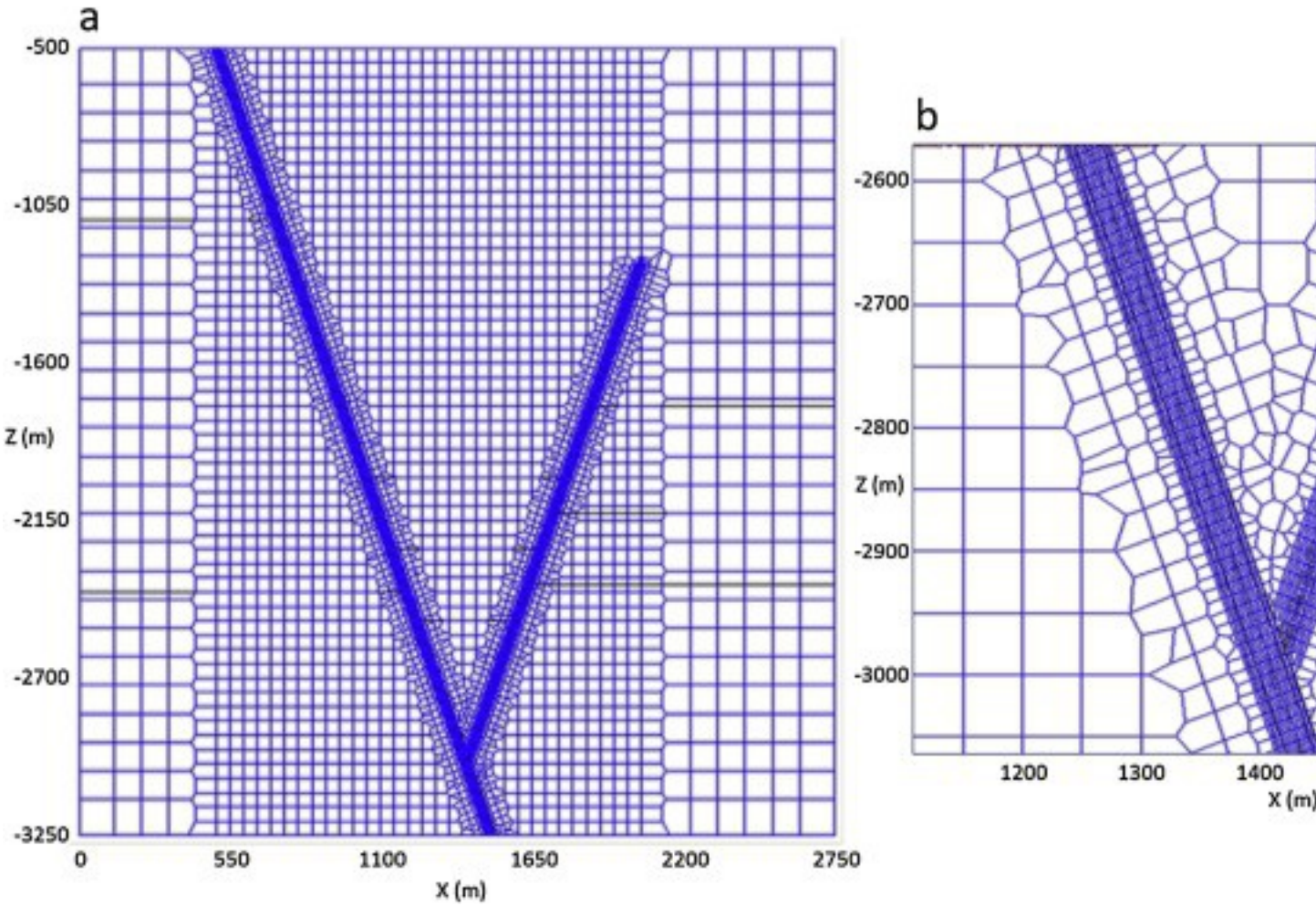

1. Download high-res image (1015KB)
2. Download full-size image

Fig. 3. Grid geometry of the 2D conceptual model domain: (a) entire view, (b) expanded veiw at the junction of the two faults. Note that the horizontal black lines in (a) indicate the boundaries of different lithologic zones.

To characterize the fault zones, we use the conceptual model of a generic fault developed by Gudmundsson et al. (2002), which contains a few meter-thick fault gouge, a slip plane within the fault gouge, and a damage zone outside the fault gouge (Fig. 4(a)). Our model includes 32.5 m-thick and 22.5 m-thick fault zones in the main and conjugate faults, respectively (Fig. 4(b)). The main fault zone has a thicker fault gouge than the conjugate fault zone has. Fault zones are conceptualized as being composed of brittle rocks and contain cracks, which provide flow pathways for fluid and heat.

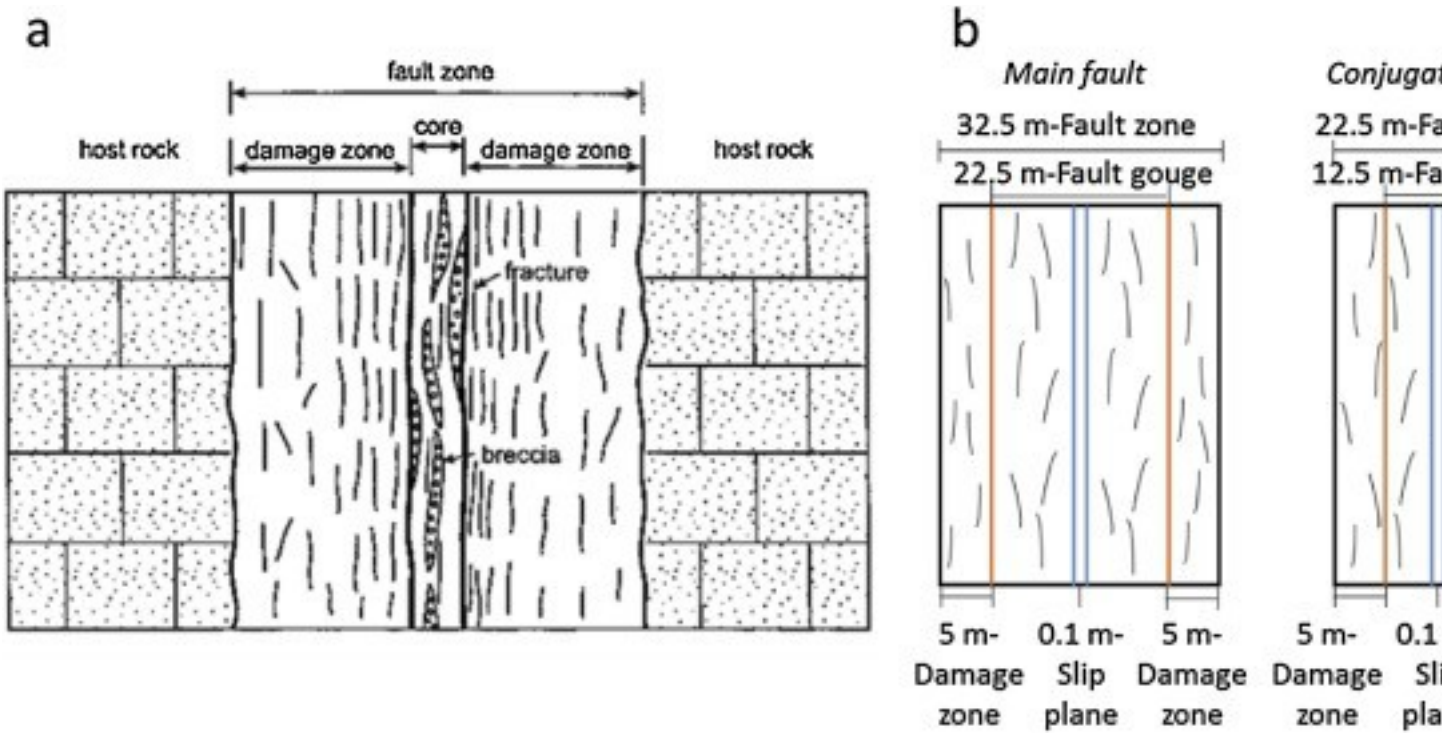

1. Download high-res image (450KB)
2. Download full-size image

Fig. 4. A generic model of a fault zone: (a) concept of a fault zone involving fractured fault gouge and damage zone (Gudmundsson et al., 2002); (b) dimensions of fault zones in our model. Note that 'G' and 'S' in the grid block containing slip plane indicate the fault gouge and slip plane, respectively.

Fig. 5 shows the initial pressure and temperature distributions. The system is initially filled with brine; and a hydrostatic pressure gradient of 9.79 kPa/m is applied. The initial temperature distribution shows the effect of rising flow of fluid and heat through the main fault, which was obtained by running a natural-state simulation, which started with the temperature distribution of Fig. 1(c), for sufficiently long time of 10^6 days to get steady-state condition. Constant pressure and temperature are set at the top boundary; and the other three sides are set at no flow condition of heat and fluid, in light of the short time of our push-pull test.

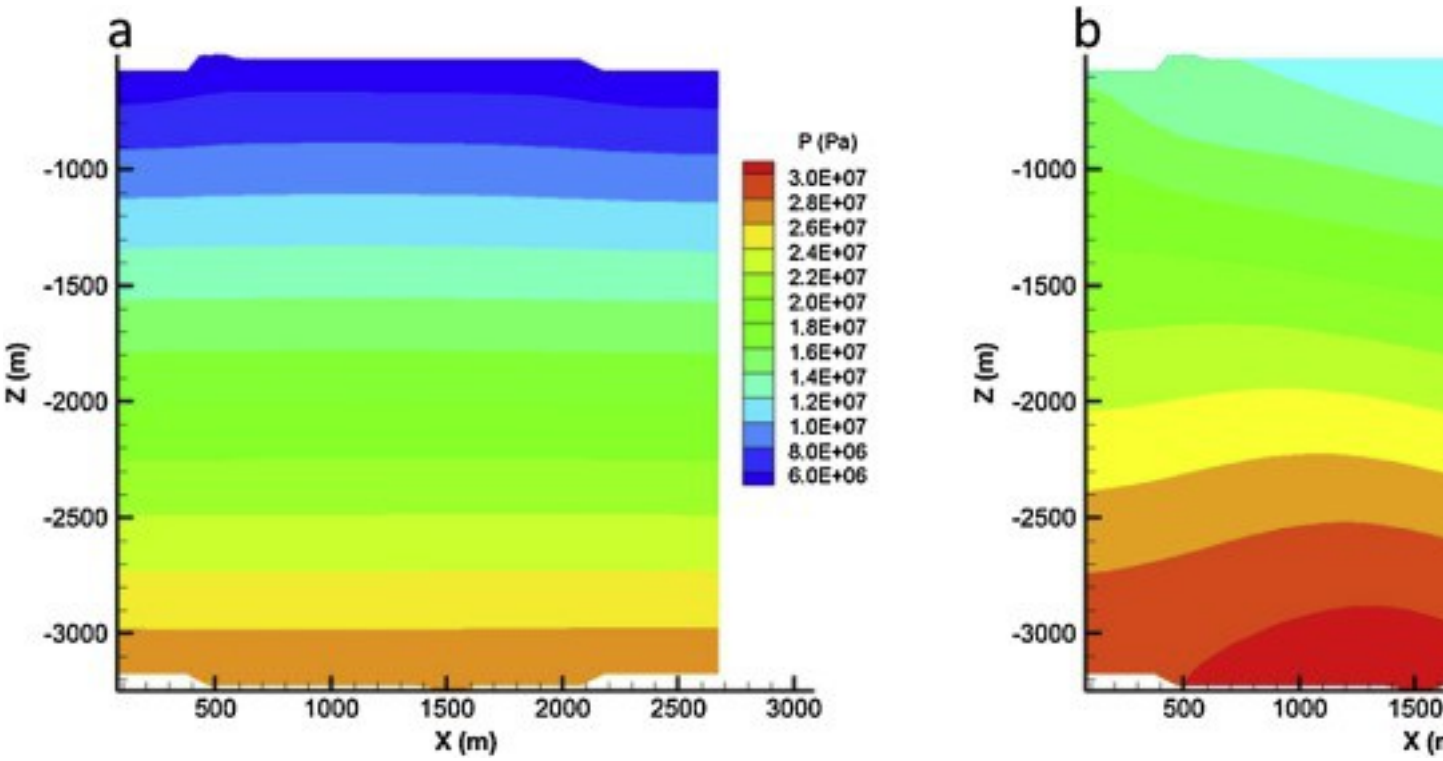

1. Download high-res image (260KB)
2. Download full-size image

Fig. 5. Reservoir initial conditions: (a) pressure distribution, (b) temperature distribution.

Hydrogeologic properties of the system for the numerical simulations are provided in Table 1. Potentially influential and unknown parameters for the flow of injected CO_2 in the fault zones are indicated with *—the absolute permeability, and the input parameters for the relative permeability and capillary pressure functions in the fault slip plane, fault gouge, and damage zone. Sensitivity and data-worth analyses will be performed for these parameters after the forward modeling section.

Table 1. Properties of the DVGS (Borgia et al., 2017; Oldenburg et al., 2016). Rock grain density = 2650 kg m^{-3}, porecompressibility = 7.25 × 10^{-12} Pa^{-1}, rock grain specific heat = 1000 J kg^{-1} K^{-1}, and formation thermal conductivity = 2.1 W m^{-1} K^{-1}, respectively. Note that $1/P_0$ is proportional to the square root of the absolute permeability.

Zone	Porosity [vol. frac.]	Permeability [m^2]	Parameters of capillary pressure	Parameters of relative permeability
Slip plane	0.30	2×10^{-1} ^{2*}	None	Corey[b], S_{lr}* = 0.3; S_{gr}* = 0.05

Zone	Porosity [vol. frac.]	Permeability [m²]	Parameters of capillary pressure	Parameters of relative permeability
Fault gouge	0.10	2×10^{-12} [c]	van Genuchten[a], $\lambda^* = 0.4438$; $S_{lr}^* = 0.30$; $S_{ls} = 1.0$; $1/P_0^* = 2.100 \times 10^{-4}$ Pa^{-1}; $P_{max} = 10^8$ Pa	Corey[b], $S_{lr}^* = 0.3$; $S_{gr}^* = 0.05$
Damage zone	0.05	2×10^{-15} [c]	van Genuchten, $\lambda^* = 0.4438$; $S_{lr}^* = 0.30$; $S_{ls} = 1.0$; $1/P_0^* = 6.641 \times 10^{-6}$ Pa^{-1}; $P_{max} = 10^8$ Pa	Corey[b], $S_{lr}^* = 0.3$; $S_{gr}^* = 0.05$
High-permeability zone	0.10	5×10^{-16}	van Genuchten, $\lambda = 0.4438$; $S_{lr} = 0.30$; $S_{ls} = 1.0$; $1/P_0 = 3.321 \times 10^{-6}$ Pa^{-1}; $P_{max} = 10^8$ Pa	Corey[b], $S_{lr}^* = 0.3$; $S_{gr}^* = 0.05$
Low-permeability zone	0.05	10^{-16}	van Genuchten, $\lambda = 0.4438$; $S_{lr} = 0.30$; $S_{ls} = 1.0$; $1/P_0 = 1.485 \times 10^{-6}$ Pa^{-1}; $P_{max} = 10^8$ Pa	Corey[b], $S_{lr}^* = 0.3$; $S_{gr}^* = 0.05$
Impermeable zone	0.01	10^{-19}	van Genuchten, $\lambda = 0.4438$; $S_{lr} = 0.30$; $S_{ls} = 1.0$; $1/P_0 = 4.696 \times 10^{-8}$ Pa^{-1}; $P_{max} = 10^8$ Pa	Corey[b], $S_{lr}^* = 0.3$; $S_{gr}^* = 0.05$

a (Van Genuchten, 1980).

b (Corey, 1954).

c We used a permeability anisotropy factor of two for the fault zone materials. Specifically, for connections in the perpendicular-to-fault direction, permeability values are 1×10^{-12} m², 1×10^{-12} m², and 1×10^{-15} m² for the slip plane, fault gouge, and damage zone, respectively.

4. Forward simulations

We simulated the processes of $scCO_2$ push-pull into the faults of DVGS by using TOUGH2-ECO2N (Pan et al., 2015), a fluid property module for mixtures of CO_2, water, and NaCl. Push and pull of $scCO_2$ continued for $t = 0$–30 days and $t = 30$–60 days, respectively. In the numerical simulations, a small mass fraction of NaCl in aqueous phase (=1×10^{-7}) was used.

In the push phase, CO_2 was injected by using a 0.3 MPa constant overpressure above the local hydrostatic pressurein the injection grid blocks in the fault slip plane and fault gouge of the main fault at Z-coordinates between −3018 m and −3024 m, which is just

below the junction of the main and conjugate faults. The injection grid blocks contain 100% CO_2. Temperature of injected CO_2 was same as the local ambient temperature of 265 °C. In the pull phase, fluid was produced by 0.3 MPa underpressure at the same locations as the injection.

Results of numerical simulations are provided in Fig. 6, Fig. 7, Fig. 8, Fig. 9, Fig. 10, Fig. 11, Fig. 12. Fig. 6 shows the distribution profiles of pressure, temperature, and gas saturation in the reservoir, after push (a–c) and pull processes (d–f). After the 30 days of push, the system pressure slightly increased along the faults (Fig. 6(a)). Similarly, system pressure slightly decreased along the faults after the subsequent 30-day pull process (Fig. 6(d)). System temperature insignificantly changed in the faults after the push and pull, as the CO_2 was injected at the ambient temperature (Fig. 6(b) and (e)). (From the preliminary simulation using lower temperature-CO_2, we still observed that the system temperature including fault planeshardly changed because of the high effective heat capacityof the formation.)

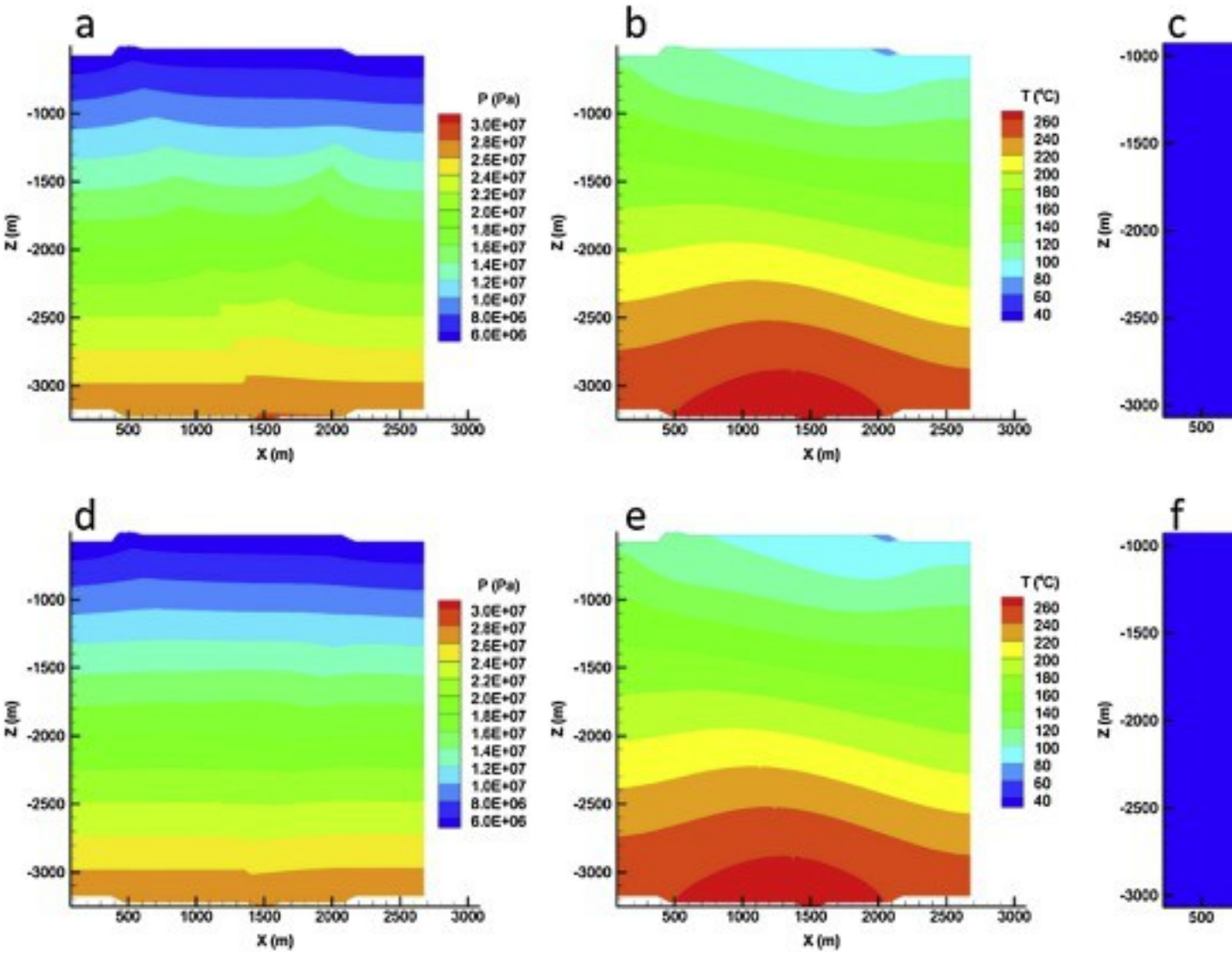

1. Download high-res image (454KB)
2. Download full-size image

Fig. 6. Reservoir profiles after 30 days-push and following 30 days of pull: (a) pressure distribution after push, (b) temperature distribution after push, (c) gas saturation distribution after push, (d) pressure distribution after pull, (e) temperature distribution after pull, (f) gas saturation distribution after pull.

Note that in the plots of gas saturation distributions (c) and (f), different extents of the domain (different *X* and *Z* limits) were used relative to those for the pressure and temperature plots.

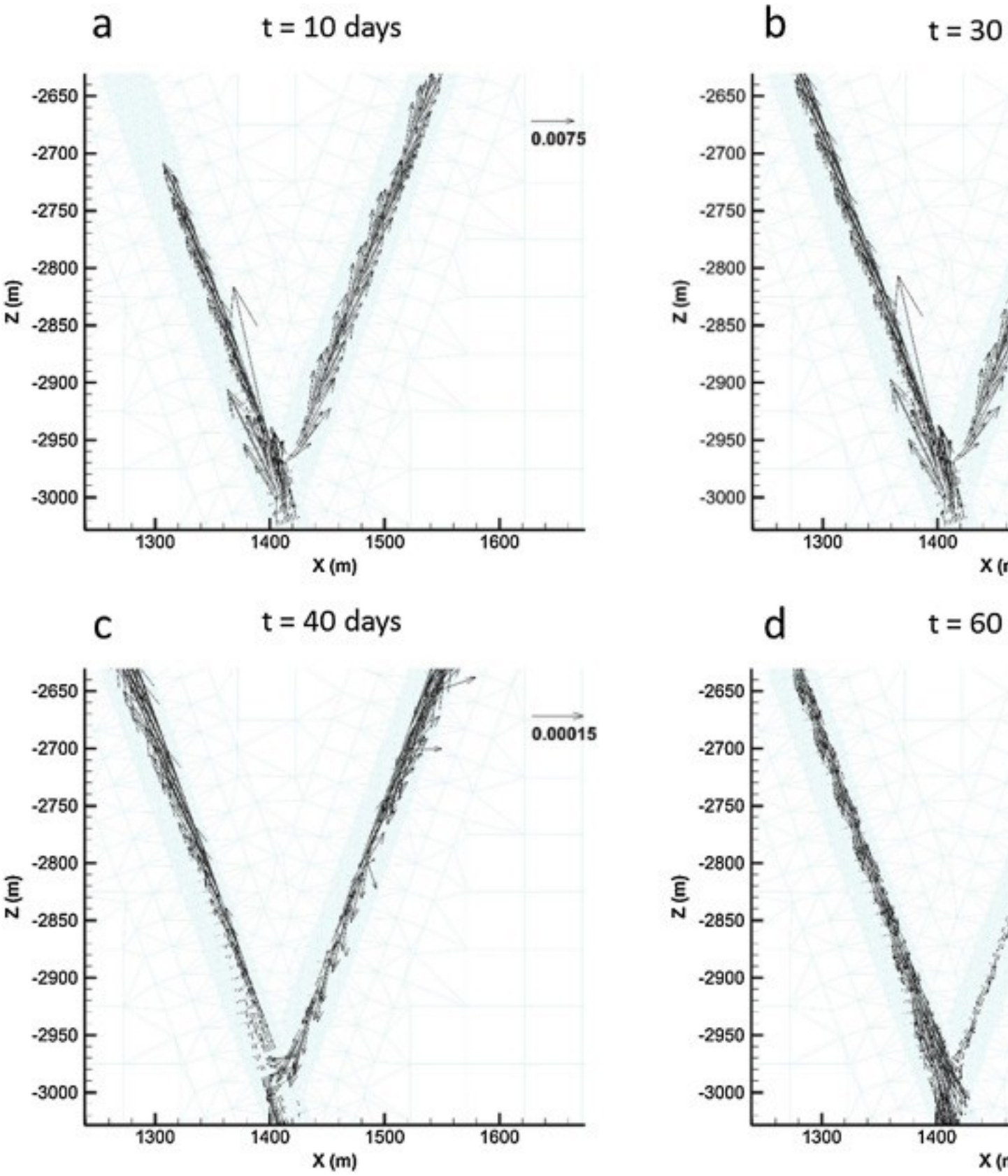
a
t = 10 days
0.0075
-2650
-2700
-2750
-2800
-2850
-2900
-2950
-3000
Z (m)
1300
1400
1500
1600
X (m)
b
t = 30
c
t = 40 days
0.00015
d
t = 60

1. Download high-res image (876KB)
2. Download full-size image

Fig. 7. Vectors of CO_2 mass flow (kg/s) during push-pull. Note that different length scales of vectors were used in push (a and b) and pull (c and d).

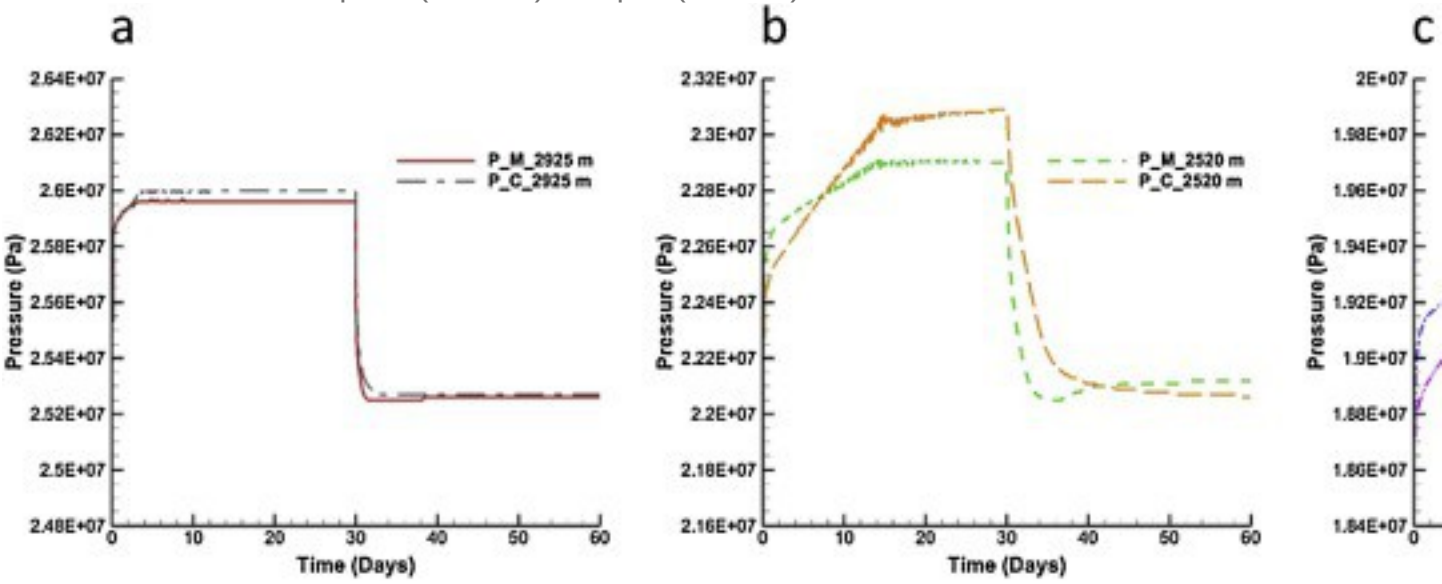

1. Download high-res image (239KB)
2. Download full-size image

Fig. 8. Observed pressure as a function of time at three different locations in the main and conjugate faults: (a) Z = −2925 m, (b) Z = −2520 m, (c) Z = −2100 m.

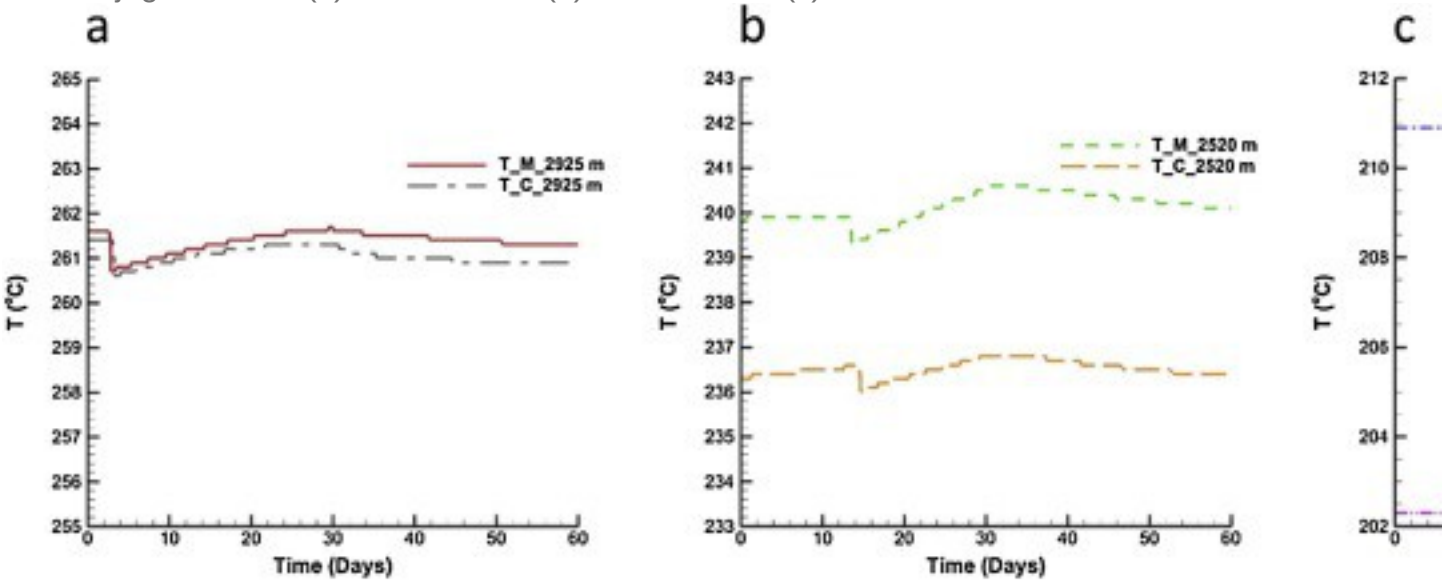

1. Download high-res image (175KB)
2. Download full-size image

Fig. 9. Observed temperature as a function of time at three different locations in the main and conjugate faults: (a) Z = −2925 m, (b) Z = −2520 m, (c) Z = −2100 m.

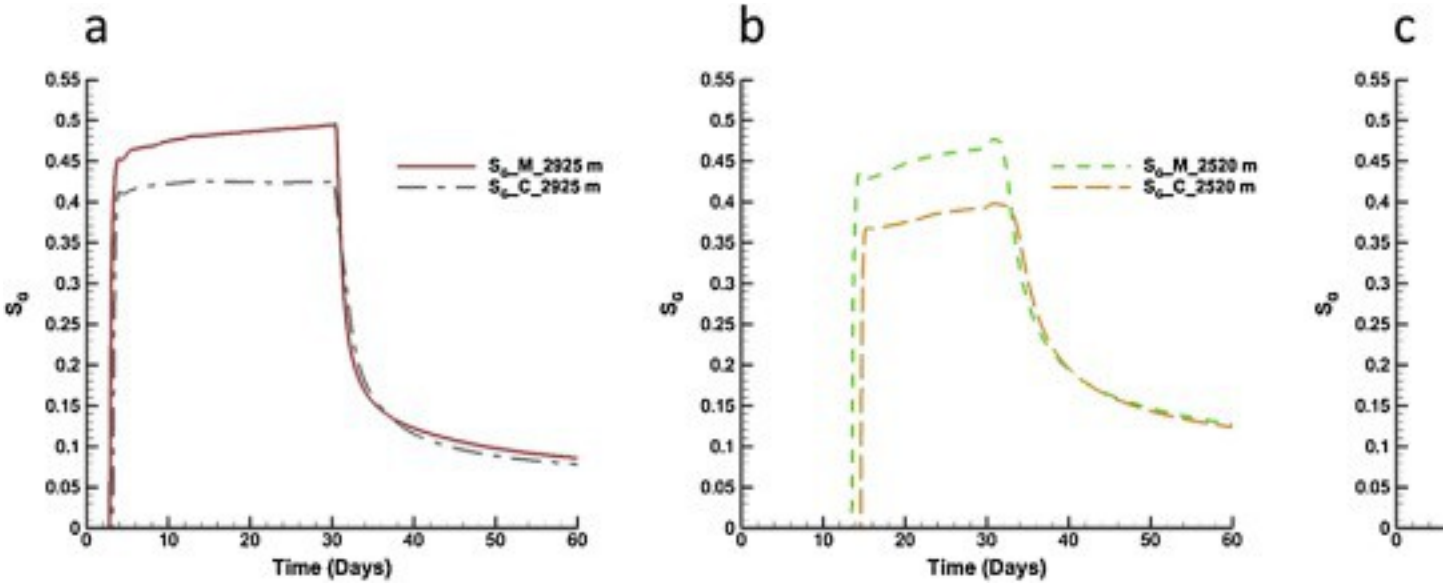

1. Download high-res image (197KB)
2. Download full-size image

Fig. 10. Observed gaseous phase saturation as a function of time at three different locations in the main and conjugate faults: (a) Z = −2925 m, (b) Z = −2520 m, (c) Z = −2100 m.

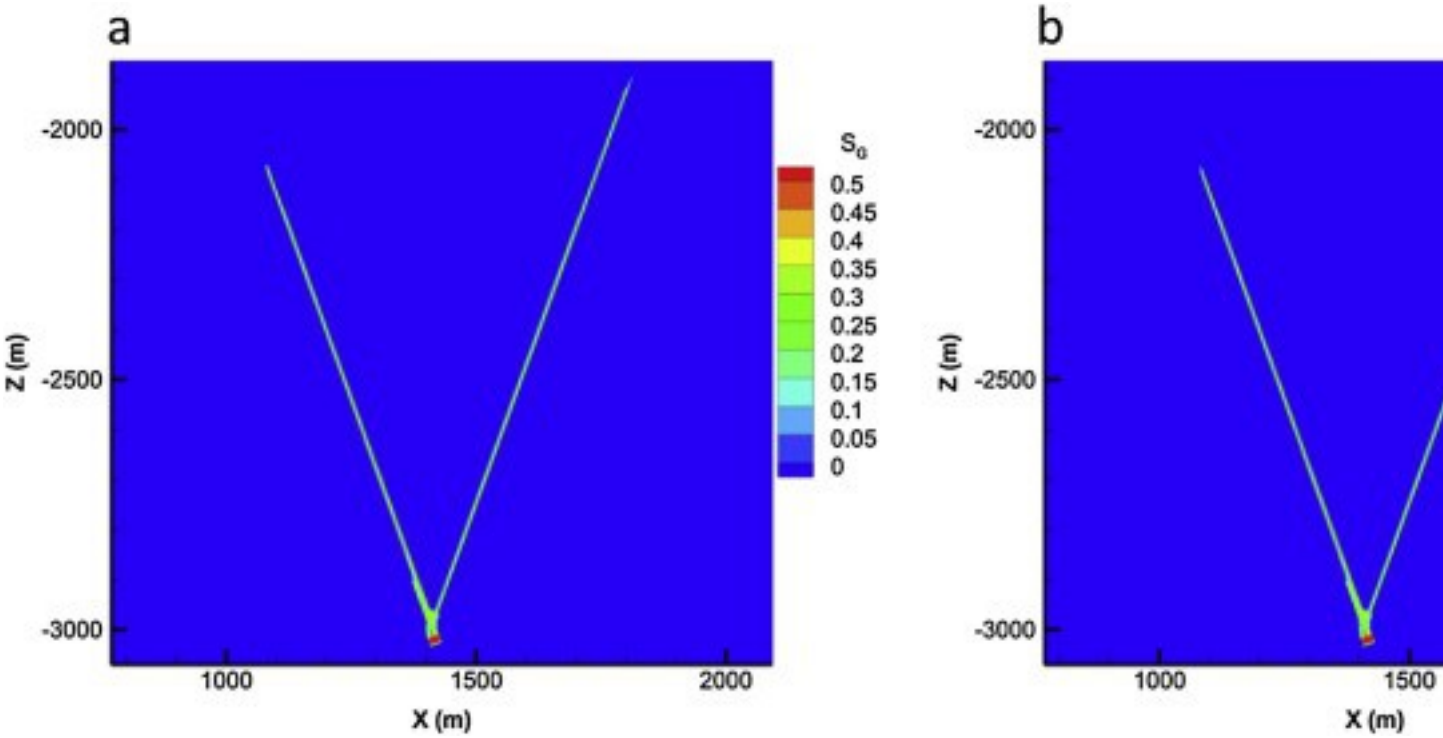

1. Download high-res image (175KB)
2. Download full-size image

Fig. 11. Gas saturation profiles after 30 days of push: (a) heterogeneous reservoir case (shown in Fig. 2), (b) homogeneous reservoir case without high-permeability zones.

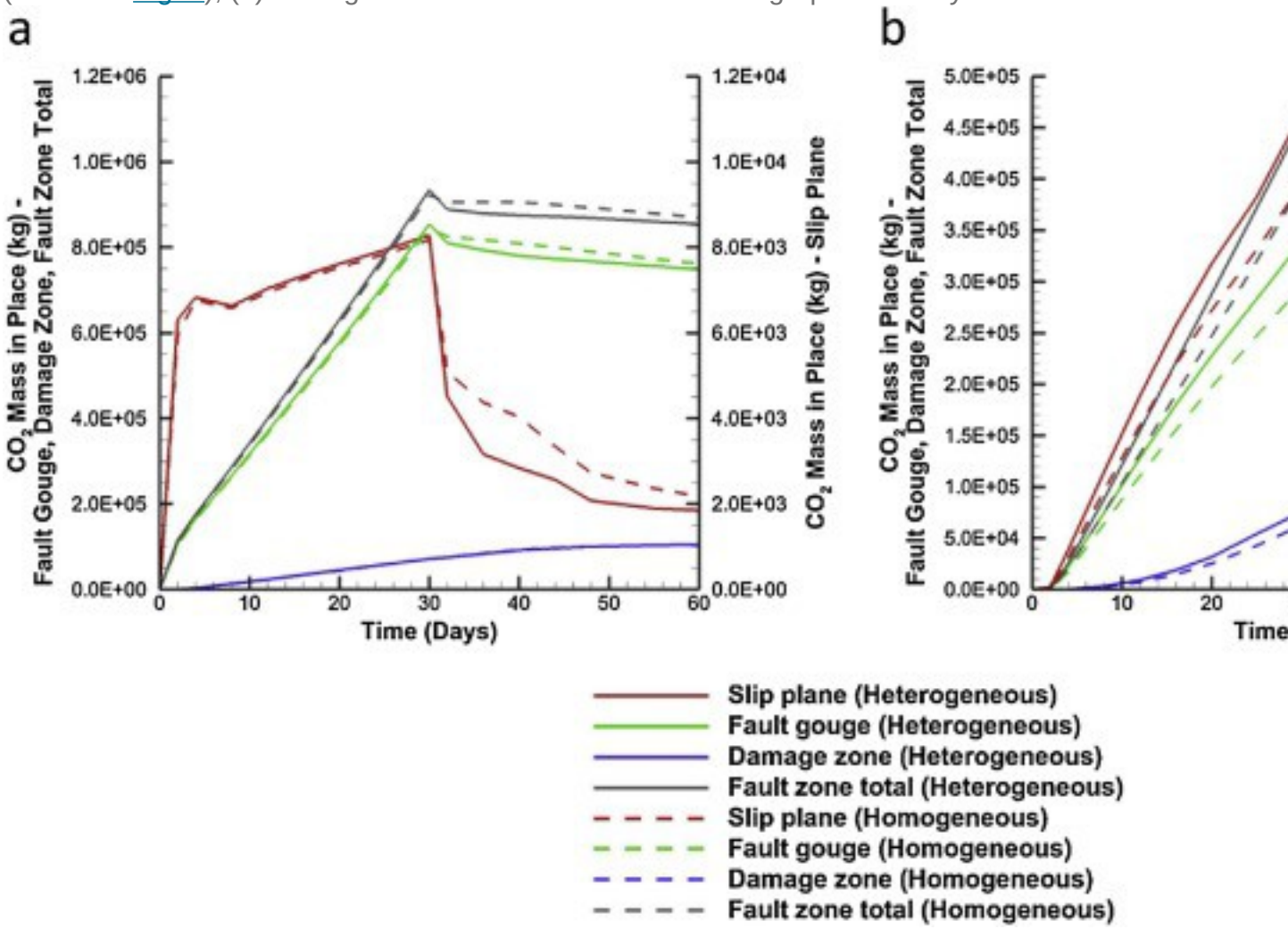

1. Download high-res image (521KB)
2. Download full-size image

Fig. 12. Total CO_2 mass in place in the fault zones during 30-day-push and 30-day pull: (a) main fault, (b) conjugate fault. Note that the thickness of the 2D model is 10 m in the *Y*-direction.

The gas saturation profiles in Fig. 6(c) show that the injected CO_2 reached upward to $Z = -2070$ m and −1890 m in the main and conjugate faults, respectively, i.e., reached a higher level in the smaller conjugate fault. Injected CO_2flowed upward more easily in the conjugate fault than in the main fault because the conjugate fault contacts formations with high permeability over a larger surface area than the main fault does, as shown in Fig. 2, providing less resistance for water in the conjugate fault to flow into the formation as it is displaced by CO_2. Accordingly, the vectors of CO_2 mass flow in Fig.

7 show that more vigorous CO_2flow was observed in the conjugate fault than in the main fault early in the push phase.
After the pull phase, CO_2 had risen by buoyancy to Z = −1345 m and −1440 m in the main and conjugate faults, respectively (Fig. 6(f)). From the CO_2 mass flow vectors in Fig. 7, it is observed that CO_2 still flowed upward in the early time period of the pull phase in both the conjugate and main faults, and slightly flowed down afterward.
We observed the pressure, temperature, and saturation of gaseous phase in the gouge of fault zones, where the most injected CO_2 passed along during push and pull. The observation positions are at three different locations at Z = −2925 m, −2520 m, and −2100 m in the main and conjugate faults. The observation results are shown in Fig. 8, Fig. 9, Fig. 10. Note that pressure in the fault zones promptly reacted to the injection and production of CO_2, while temperature and saturation of gaseous phase reacted slower than pressure did.
In order to examine the effects of the low-permeability and high-permeability (brittle) zones surrounding the fault zone, we performed a simulation of push-pull assuming a homogeneous reservoir of low permeability. The gas saturation profiles of the heterogeneous (original) case and the homogeneous low-permeability case are shown in Fig. 11. In the homogeneous reservoir case, injected CO_2reached Z = −2060 m and −2040 m in the main and conjugate faults, respectively.
Fig. 12 shows the CO_2 mass in place during push-pull in the fault zones. Both in the main and conjugate faults, the majority of injected CO_2 flowed into the fault gouge during the push phase. During the pull phase, the majority of CO_2flowed upward through the damage zone driven by buoyancy effects, and only a small amount of CO_2 was produced through the fault slip plane and fault gouge. Comparing the cases of heterogeneous and homogeneous rock, we observe that the existence of highly permeable zones significantly affected the CO_2 flow in the fault zones during push and pull, especially in the conjugate fault.

5. Sensitivity and data-worth analyses

We use the PEST protocol of iTOUGH2 to perform sensitivity and data-worth analyses, along with the forward simulation of TOUGH2-ECO2N (Finsterle, 1999; Finsterle and Zhang, 2011). We conduct a formal sensitivity analysisof system responses in the fault zones to the unknown parameters shown in Table 1. From the formal sensitivity analysis, we determine the most influential unknown parameters and the most sensitive system responses. Next, we conduct data-worth analysis to determine the most

valuable data to be measured for better prediction of CO_2distribution in the fault zones, with respect to the influential unknown parameters.

5.1. Formal sensitivity analysis

We performed a set of formal sensitivity analyses for the push and pull processes. Both processes are continued for 30 days using constant pressure of injection (+0.3 MPa) and production (-0.3 MPa). By perturbing unknown parameters, we observe system responses and compute the scaled sensitivity coefficients described as:

(1)$\bar{S}ij=\partial zi\partial pj\cdot\sigma pj\sigma zi$

(Wainwright and Finsterle, 2016) where, $\bar{S}ij$ is the scaled sensitivity; $\partial zi/\partial pj$ is the partial derivative of output variable (z_i) with respect to the unknown parameter (p_j); $\sigma pj$is the parameter scaling factor, which can be a parameter variation or standard deviation; and σzi is the output scaling factor, which can be an expected uncertainty of output. The initial values and the scaling factors of parameters are listed in Table 2. There are 15 unknown values in the fault zones; and the scaled sensitivity coefficients of measurable system responses to the parameters are computed. We observe the following system responses using geothermal well logging tools: pressure and temperature at three different locations at Z = −2925 m, −2520 m, and −2100 m in the main fault and conjugate fault. The system responses were measured from 2 days to 30 days with a measurement frequency of 1 day, both in push and pull. Scaling factors of pressure and temperature were 1×10^4 Pa and 0.5 °C, respectively (Steingrímsson, 2013). (Considering that the two measurement points at Z = −2520 m in the main fault and Z = −2925 m in the conjugate fault would already be drilled (Fig. 1), four more wells would be needed for the additional measurements. Drilling wells for such monitoring will generate cost, and these additional costs for drilling have not been addressed in this study. Note further that the kind of data-worth analysis demonstrated here can be used to minimize the number of additional wells and monitoring points needed to constrain various fault-zone properties.)

Table 2. Initial value (and variation in parentheses) of 15 unknown parameters. Note that the absolute permeability (K) is in Log distribution, and the variation of $Log_{10}(K)$ is indicated. No capillary pressure is considered in the fault slip planes. Note that $1/P_0$ is proportional to the square root of the absolute permeability.

Parameters	Slip plane	Fault gouge	Damage zone
$\mathbf{Log_{10}(K[m^2])}$	−11.699 (0.2)	−11.699 (0.2)	−14.699 (0.2)
S_{lr}	0.30 (0.05)	0.30 (0.05)	0.30 (0.05)

Parameters	Slip plane	Fault gouge	Damage zone
S_{gr}	0.05 (0.05)	0.05 (0.05)	0.05 (0.05)
λ	None	0.4438 (0.1)	0.4438 (0.1)
$1/P_0$ [Pa^{-1}]	None	2.100×10^{-4}(1.0×10^{-4})	6.641×10^{-6}(3.32×10^{-6})

As results of formal sensitivity analysis after push and pull processes, Table 3 shows the sum of absolute scaled sensitivity coefficients, which were obtained from 2 days to 30 days with a measurement frequency of 1 day. For each parameter and output response, the sum was computed as follows.

(2)$\bar{S}j,sum=\sum foralli,t|\bar{S}ij,t|$

(3)$\bar{S}i,sum=\sum forallj,t|\bar{S}ij,t|$

where, $\bar{S}j,sum$ is the sum of scaled sensitivity coefficients of parameter p_j; $\bar{S}i,sum$ is the sum of scaled sensitivity coefficients of output response z_i; and $\bar{S}ij,t$ is the scaled sensitivity coefficient of z_i to p_j obtained at each measurement time t, respectively.

Table 3. Sum of scaled sensitivity coefficients in descending order during the push and pull processes.

Parameters	Push	Parameters	Pull	Output responses	Push	Output responses	Pull
$1/P_{0\_FG}$	4142.86	S_{gr_FG}	1320.00	P_{M_2100m}	4280.89	P_{M_2100m}	1988.90
λ_{FG}	2140.60	$1/P_{0\_FG}$	942.86	P_{C_2100m}	3868.49	P_{C_2100m}	1821.98
S_{gr_FG}	1280.00	S_{gr_FS}	700.00	P_{M_2520m}	3102.24	P_{C_2520m}	894.35
S_{lr_FG}	1270.00	S_{gr_DZ}	370.25	P_{C_2520m}	1697.08	P_{C_2925m}	725.66
S_{gr_FS}	1220.00	K_{DZ}	462.82	P_{M_2925m}	927.11	P_{M_2520m}	698.18
K_{DZ}	1082.99	S_{lr_FG}	410.00	P_{C_2925m}	372.30	T_{C_2520m}	65.42
K_{FG}	971.91	$1/P_{0\_DZ}$	399.94	T_{C_2520m}	117.70	T_{C_2100m}	14.03
K_{FS}	860.84	λ_{FG}	360.52	T_{C_2925m}	68.78	T_{M_2100m}	11.17
$1/P_{0\_DZ}$	749.89	K_{FG}	370.25	T_{M_2925m}	32.86	P_{M_2925m}	0.00
S_{lr_FS}	403.33	K_{FS}	323.97	T_{C_2100m}	13.76	T_{M_2520m}	0.00
λ_{DZ}	31.996	S_{lr_DZ}	116.67	T_{M_2520m}	7.84	T_{M_2925m}	0.00
S_{lr_DZ}	50.00	λ_{DZ}	112.66	T_{M_2100m}	3.33	T_{C_2925m}	0.00
S_{gr_DZ}	0.00	S_{lr_FS}	399.94				

From the sum of scaled sensitivity coefficients, we can narrow down the most influential unknown parameters in the push and pull phases. In the push phase, we select the five most influential unknown parameters—capillary pressure parameters in fault gouge

($1/P_{0\_FG}$, λ_{FG}), irreducible saturations of gaseous phase and liquid (aqueous) phase in fault gouge (S_{gr_FG}, S_{lr_FG}), and irreducible saturation of gaseous phase in fault slip plane (S_{gr_FS}). In the pull phase, the five most influential unknown parameters are irreducible saturation of gaseous phase in fault gouge (S_{gr_FG}), capillary pressure parameter in fault gouge ($1/P_{0\_FG}$), irreducible saturation of gaseous phase in fault gouge and damage zone (S_{gr_FG}, S_{gr_DZ}), and permeability in damage zone (K_{DZ}).
From the sum of scaled sensitivity coefficients of output responses, we find that pressure is much more sensitive than temperature to the unknown parameters, both in push and pull.

In the next section of data-worth analysis, the most influential parameters will be used to predict the uncertainty of CO_2 distribution in the faults. We will also analyze the impact of monitoring time for data observation and measurement uncertainty on the relative data worth of each data set.

5.2. Data-worth analysis

Data-worth analysis estimates the value of each measurement point by conducting a formal sensitivity analysis with respect to unknown parameters (Finsterle, 2015; Wainwright and Finsterle, 2016). It can be used either in the evaluation of the worth of calibration data to reduce the uncertainty of parameter estimation, or to reduce the prediction uncertainty. In this study, we apply the data-worth analysis to reduce the prediction uncertainty of CO_2distributions in the fault zones.
The procedure for the data-worth analysis is as follows (Finsterle, 2015; Wainwright and Finsterle, 2016):

1)
Select observable variables to be calculated by the forward model.

2)
Select parameters affecting the prediction of interest.

3)
By running forward simulations, evaluate the sensitivity coefficients, ∂zi/∂pj of all observations and predictions.

4)
Evaluate the covariance matrix of the estimated parameters, C_{pp}, using the following equation.

(4)Cpp=s02(JTCzz−1J)−1

where, s02 is the estimated error variance, which is set to 1 in cases without actually measured data; *J* is the Jacobian matrix, which contains the sensitivity coefficients of ∂zi/∂pj. C_{zz} is the covariance matrix of measurement errors and expected errors of predictions (σzi), which has σzi as its diagonal components.

1)

Propagate the uncertainty of the estimated parameters, C_{pp}, to the uncertainty of predictions,

(5)Cz^z^=J^CppJ^T

where, J^ is the Jacobian matrix only involving sensitivity coefficients of the predictions.

1)

Remove one actual observation datum labeled *k* and re-estimate the covariance matrix of parameter, $C_{pp,-k}$.

2)

Re-evaluate the covariance matrix of the model predictions, Cz^z^,−k.

3)

Scale the prediction matrices by using the acceptable prediction uncertainty and get C¯z^z^ and C¯z^z^,−k.

4)

Evaluate the data-worth as a relative increase of prediction uncertainty by removing the existing observation data as in the following equation:

(6)ω−k=1−tr(C¯z^z^)tr(C¯z^z^,−k)

where, ω_{-k} is the data worth of observation data labeled *k*; “tr” gives the trace of matrix, which is the sum of the diagonal components.

In step (1), the observable variables were categorized into the actual observations and predictions. In our case, the actual observations were the pressure and temperature in the fault zones. The prediction variables were the CO_2distributions in the fault zones, which were described by using the gaseous phase saturation in a two-phase condition. We measured the observation variables starting from t = 2 days until t = 20 days with a measurement frequency of 1 day, and predicted the CO_2 distributions in the fault zones at 30 days, in each case of push and pull.

For step (2), we already selected the most influential unknown parameters affecting observation variables from the previous sensitivity analysis. In step (3), these influential parameters were perturbed, and the variable observations and predictions were

calculated. Because we selected the five most influential parameters, six forward simulation runs including one unperturbed standard case plus five perturbed-parameter cases were performed in each of data-worth analyses in the push and pull phases.

The results of data-worth analysis are provided in Table 4and Fig. 13. In the push phase, P_{M_2520m} showed the highest data worth for reducing prediction uncertainty, followed by P_{C_2520m}, P_{C_2100m}, and P_{M_2100m}. By summing up the data-worth values, we found that the measurement of these four observation data reduced the prediction uncertainly by 86.45%. In addition to these four observations, measurement of P_{M_2925m} reduced the prediction uncertainty even more. The measurement of temperature was not necessarily recommended for the reduction of prediction uncertainty, owing to their low data-worth values. The reason for this result is the much higher sensitivity coefficients of pressure than temperature, which arise because of the faster and more active response of pressure relative to temperature during the push process, as can be seen in Fig. 10.

Table 4. Results of the data-worth analysis in descending order. Note that the observation was made every 1 day starting from t = 2 days until t = 20 days, in both push and pull phases. Also note that the sum of all data-worth is 1 (=100%).

Observation data	**Data worth (ω_{-k}) in push [%]**	**Observation data**	**Data worth (ω_{-k}) in pull [%]**
$\boldsymbol{P_{M\_2520m}}$	38.81	P_{C_2100m}	50.71
$\boldsymbol{P_{C\_2520m}}$	16.73	P_{M_2100m}	19.32
$\boldsymbol{P_{C\_2100m}}$	16.52	P_{C_2520m}	17.82
$\boldsymbol{P_{M\_2100m}}$	14.39	P_{M_2520m}	12.12
$\boldsymbol{P_{M\_2925m}}$	11.15	T_{M_2520m}	0.01
$\boldsymbol{P_{C\_2925m}}$	2.29	T_{C_2100m}	0.01
$\boldsymbol{T_{C\_2925m}}$	0.11	P_{M_2925m}	0.00
$\boldsymbol{T_{M\_2100m}}$	0.00	P_{C_2925m}	0.00
$\boldsymbol{T_{M\_2520m}}$	0.00	T_{M_2100m}	0.00
$\boldsymbol{T_{M\_2925m}}$	0.00	T_{M_2925m}	0.00
$\boldsymbol{T_{C\_2100m}}$	0.00	T_{C_2520m}	0.00
$\boldsymbol{T_{C\_2520m}}$	0.00	T_{C_2520m}	0.00

a

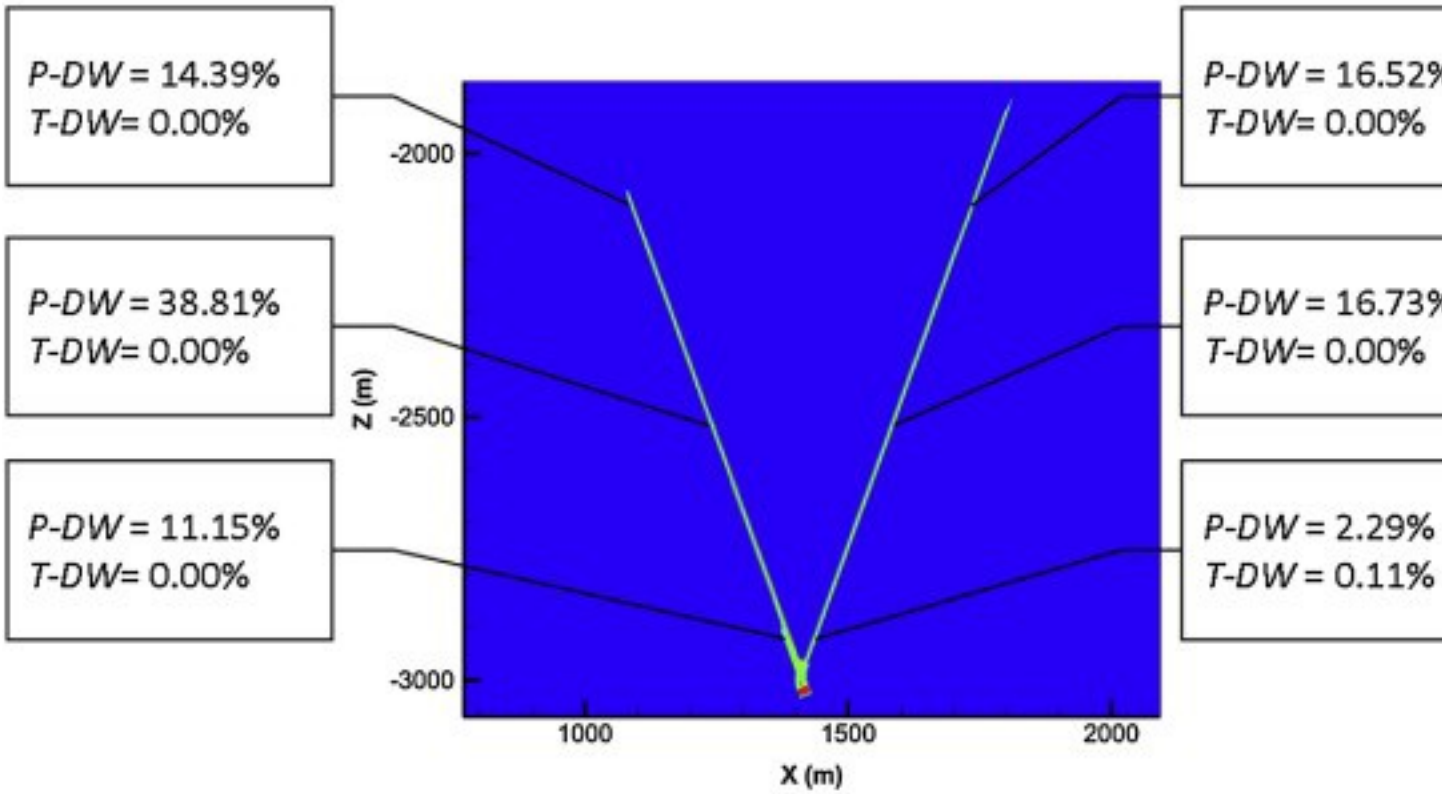
P-DW = 14.39%
T-DW= 0.00%
P-DW = 38.81%
T-DW= 0.00%
P-DW = 11.15%
T-DW= 0.00%
P-DW = 16.52%
T-DW= 0.00%
P-DW = 16.73%
T-DW= 0.00%
P-DW = 2.29%
T-DW = 0.11%
-2000
-2500
-3000
Z (m)
1000
1500
2000
X (m)

b

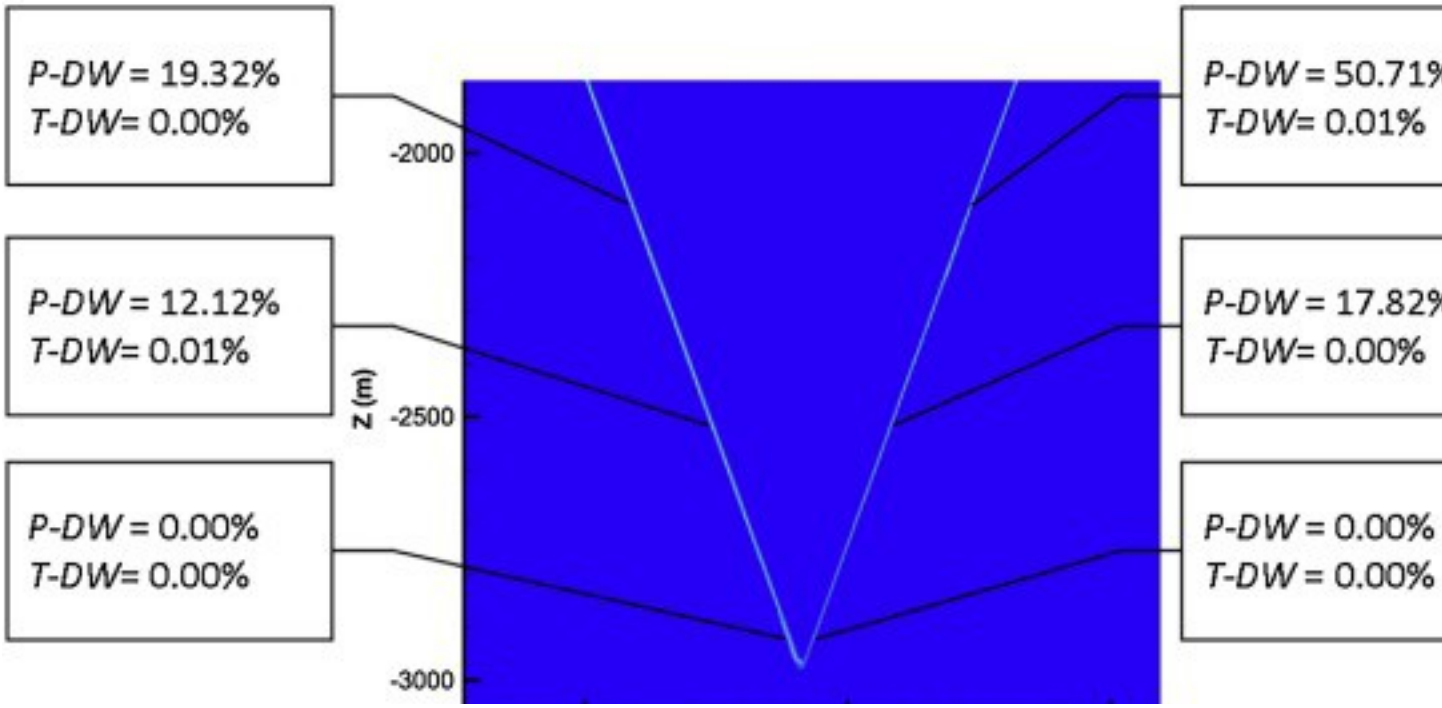
P-DW = 19.32%
T-DW= 0.00%
P-DW = 12.12%
T-DW= 0.01%
P-DW = 0.00%
T-DW= 0.00%
P-DW = 50.71%
T-DW= 0.01%
P-DW = 17.82%
T-DW= 0.00%
P-DW = 0.00%
T-DW = 0.00%
-2000
-2500
-3000
Z (m)

1. Download high-res image (458KB)
2. Download full-size image

Fig. 13. Data worth values at each observation point: (a) in push phase, (b) in pull phase. The plots of domain were obtained from the profiles of gas saturation distributions after push and pull, respectively.

In the pull phase, P_{C_2100m} showed the highest data worth, followed by P_{M_2100m}, P_{C_2520mm}, and P_{M_2520m}. The measurement of these four observation data reduced the prediction uncertainly by 99.97%. Other measurement data showed insignificant data worth below 0.01%.

Note that the results of data-worth analysis are significantly affected by the objective of the data-worth analysis. Specifically, if the objective is the reduction of estimation uncertainty of parameters, the data worth of measurement would be quite different.

Table 5 shows the output predictions and prediction uncertainty obtained by the data-worth analysis. Selection of the measurement data and measurement time will be significantly affected by the allowable prediction uncertainty. The most uncertain predictions were of $S_{G\_M\_2100m}$ and $S_{G\_C\_2925m}$ as noted by their highest standard deviations after push and pull phases, respectively.

Table 5. Output predictions of gaseous phase saturation in the faults after push and pull, and prediction uncertainty indicated by standard deviations.

Output prediction	Prediction at t = 30 days (after push)	Standard deviation (after push)	Prediction at t = 60 days (after pull)	Standard deviation (after pull)
$S_{G\_M\_2100m}$	0.0016	2.701E-02	0.1542	2.051E-04
$S_{G\_M\_2520m}$	0.4534	4.793E-04	0.1327	2.408E-04
$S_{G\_M\_2925m}$	0.4624	5.194E-04	0.0865	2.649E-04
$S_{G\_C\_2100m}$	0.2887	5.585E-04	0.1434	2.321E-04
$S_{G\_C\_2520m}$	0.2666	6.168E-04	0.1233	2.388E-04
$S_{G\_C\_2925m}$	0.2465	5.719E-04	0.0800	2.729E-04

To see the effect of monitoring time for data measurement, we conducted data-worth analysis of push and pull processes with variable monitoring times: starting from 2 days until 12 days, 16 days, 20 days (standard case), and 24 days, with a measurement frequency of 1 day. Fig. 14shows the evolution of pressure data worth during push and pull, as a function of monitoring time. In the push phase, P_{C_2100m} and P_{M_2520m} showed the biggest increase and the biggest decrease in data worth with increasing monitoring

time, respectively. In the pull phase, P_{C_2100m} and P_{M_2100m} showed the biggest increase and the biggest decrease in data worth with increasing monitoring time, respectively.

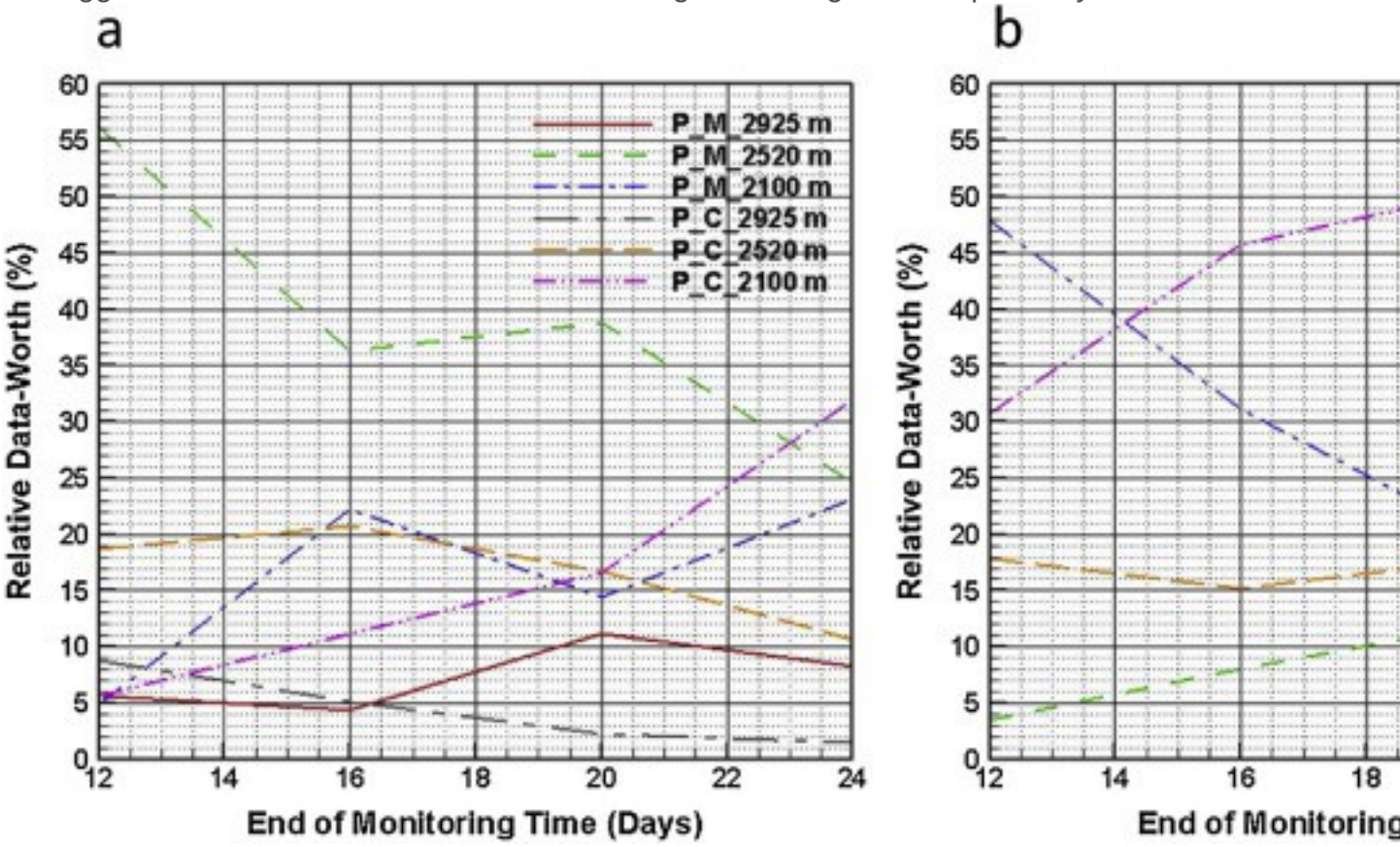

1. Download high-res image (1MB)
2. Download full-size image

Fig. 14. Data worth of pressure observation in the fault zones as a function of monitoring time: (a) push phase, (b) pull phase.

Table 6 shows the evolution of temperature data worth during push and pull, as a function of monitoring time. In overall, data worth of temperature measurement was insignificant throughout all cases of different monitoring times.

Table 6. Data worth of temperature observation in the fault zones as a function of monitoring time.

Observation data	End of monitoring time (Push)				End of monitoring time (Pull)			
	t = 12days	t = 16days	t = 20days	t = 24days	t = 12days	t = 16days	t = 20days	t = 24days
T_{M_2100m}	0.00	0.00	0.00	0.00	0.00	0.00	0.00	0.00
T_{M_2520m}	0.00	0.00	0.00	0.00	0.00	0.00	0.01	0.01
T_{M_2925m}	0.00	0.00	0.00	0.00	0.00	0.00	0.00	0.00
T_{C_2100m}	0.00	0.00	0.00	0.00	0.00	0.01	0.01	0.01
T_{C_2520m}	0.00	0.00	0.00	0.01	0.00	0.00	0.00	0.00

Observation data	End of monitoring time (Push)				End of monitoring time (Pull)			
	t = 12days	t = 16days	t = 20days	t = 24days	t = 12days	t = 16days	t = 20days	t = 24days
T_{C_2925m}	0.20	0.12	0.11	0.07	0.00	0.00	0.00	0.00

Fig. 15 shows the evolution of prediction uncertainty of gaseous phase saturation in the fault zones. Prediction uncertainty is indicated by the standard deviation of predictions. We observe the monotonic decrease of prediction uncertainty with increasing monitoring time. The prediction uncertainty was generally higher in the push phase than the pull phase, because the system output responses were more sensitive to the unknown parameters in the push phase as shown in Table 3. Note that the prediction uncertainty of $S_{G\_M\_2100m}$ was much higher than the other predictions in the push phase, as can be seen in Table 5 as well. This was because the injected CO_2approached Z = −2070 m in the main fault after the push, and $S_{G\_M\_2100m}$ was very sensitive to the unknown parameters.

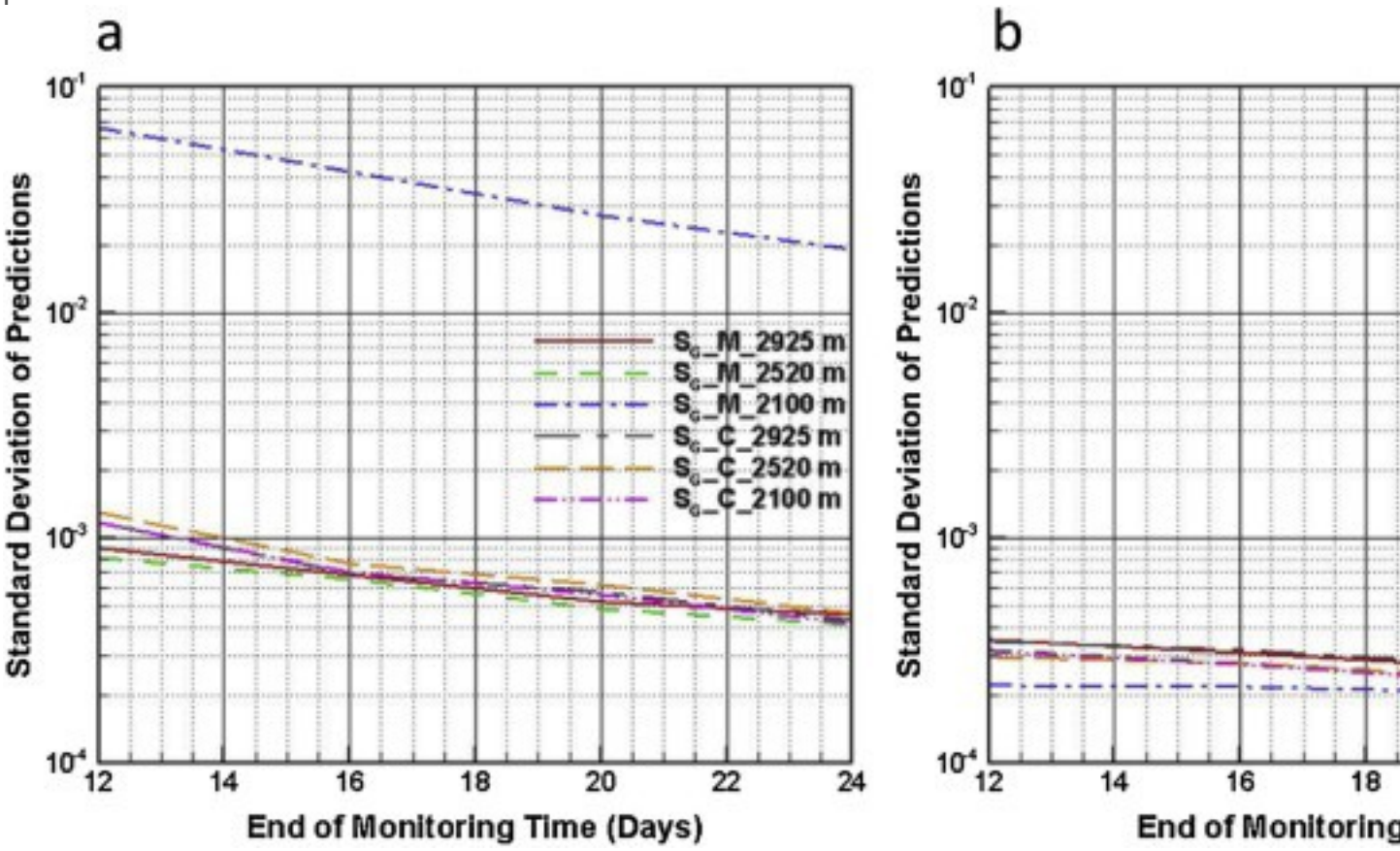

1. Download high-res image (815KB)
2. Download full-size image

Fig. 15. Prediction uncertainty as a function of monitoring time: (a) push phase, (b) pull phase.

Next we show results of data-worth analysis with variable measurement uncertainty of observation data. We conducted data-worth analysis of push and pull processes with variable measurement error of pressure measurement, because the pressure measurement turned out to be very important. We used the values of 1.0×10^4 Pa (standard case), 1.5×10^4 Pa, and 2.0×10^4 Pa for the measurement error of pressure. Fig. 16 shows the changing data worth of temperature observations with respect to the measurement error of pressure. T_{C_2925m} in the push phase and T_{C_2100m} and T_{M_2520m} in the pull phase showed increasing data worth with increasing measurement error of pressure observation, respectively, but their data worth remained insignificant throughout all cases of different measurement errors of pressure observation.

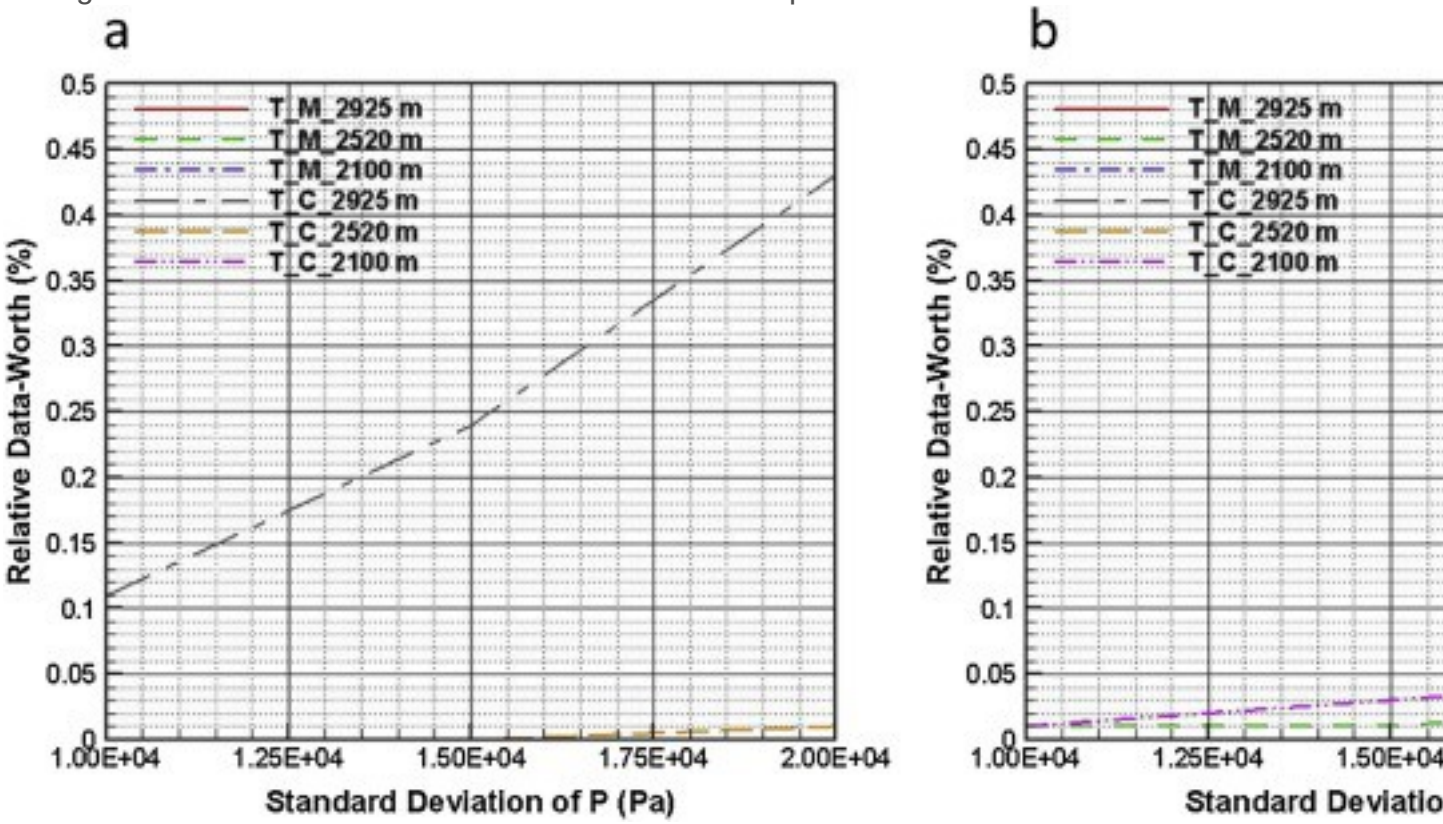

1. Download high-res image (1006KB)
2. Download full-size image

Fig. 16. Data worth of temperature observation in the fault zones as a function of measurement uncertainty of pressure observation: (a) push phase, (b) pull phase.

Table 7 shows the evolution of pressure data worth during push and pull, as a function of measurement error of pressure observation. Data worth of each pressure observation slightly decreased with its increasing measurement error.

Table 7. Data worth of pressure observation in the fault zones as a function of its measurement uncertainty. Note that the data worth of P_{C_2520m} showed slight increase with increasing measurement uncertainty, which resulted from decrease of the other observations of pressure.

Observation data	Measurement uncertainty of pressure (Pa)			Measurement uncertainty of pressure (Pa)		
	1.0×10^4	1.5×10^4	2.0×10^4	1.0×10^4	1.5×10^4	2.0×10^4
P_{M_2100m}	14.39	14.38	14.36	19.32	19.32	19.32
P_{M_2520m}	38.81	38.74	38.65	12.12	12.12	12.12
P_{M_2925m}	11.15	11.14	11.13	0.00	0.00	0.00
P_{C_2100m}	16.52	16.46	16.38	50.71	50.71	50.71
P_{C_2520m}	16.73	16.75	16.77	17.82	17.80	17.77
P_{C_2925m}	2.29	2.29	2.28	0.00	0.00	0.00

Fig. 17 shows the evolution of prediction uncertainty of gaseous phase saturation in the fault zones. We observe the monotonic increase of prediction uncertainty with increasing measurement error of pressure. As we observed in the cases of different monitoring times, it's found that the prediction uncertainty of $S_{G\_M\_2100m}$ was much higher than the other predictions in the push phase, throughout all cases of different measurement errors of pressure.

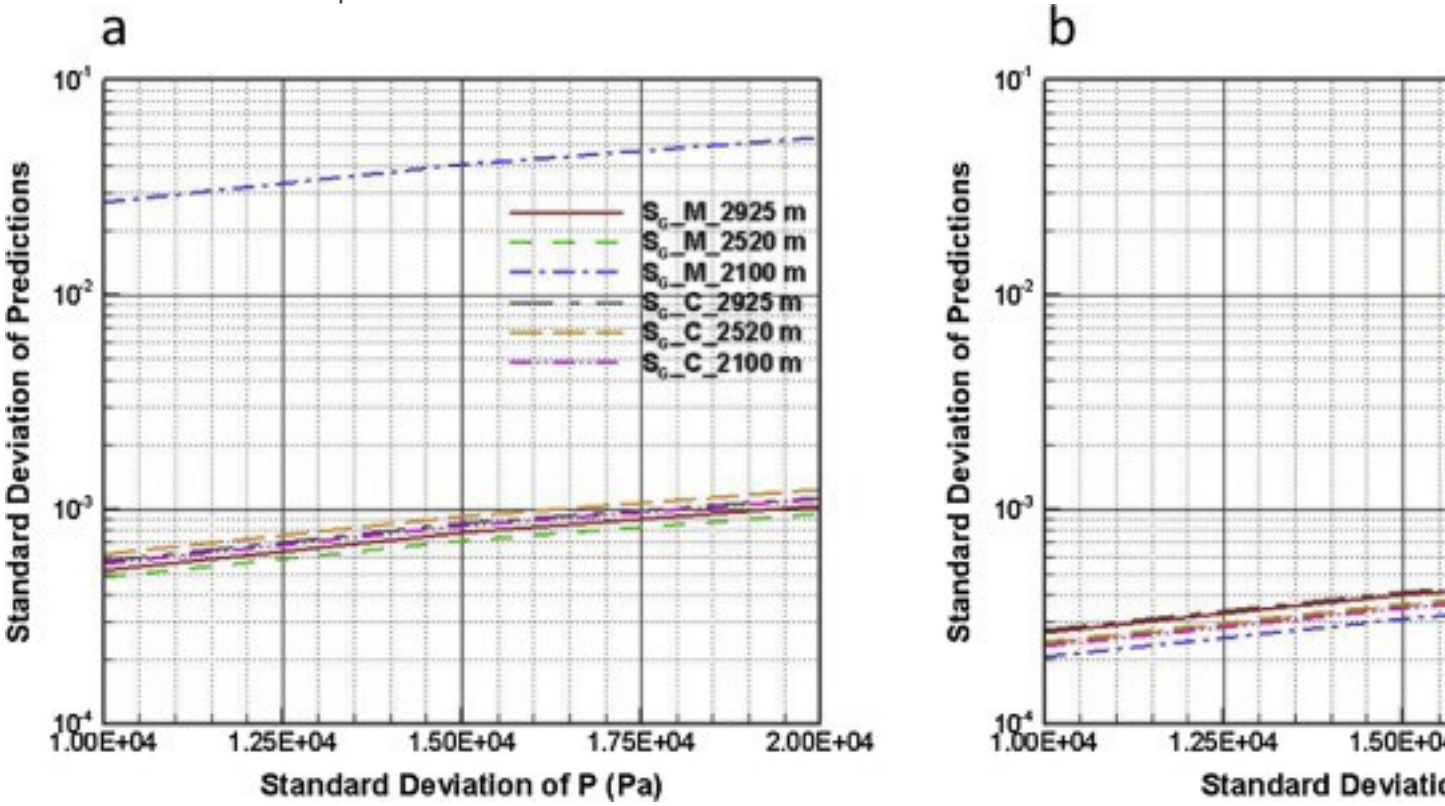

1. Download high-res image (731KB)

2. Download full-size image

Fig. 17. Prediction uncertainty as a function of measurement uncertainty of pressure observation: (a) push phase, (b) pull phase.

6. Conclusions

In this study, we investigated the technical feasibility of $scCO_2$ push-pull testing in a conjugate fault system modeled after the EGS site in Dixie Valley, Nevada, USA. We performed forward numerical simulations of $scCO_2$push-pull processes that could be carried out to emplace CO_2 as a contrast agent for seismic and well-loggingcharacterization of the fault zones. Along with the forward simulations, we performed sensitivity analysis and data-worth analysis. From the formal sensitivity analysis, we determined the most influential parameters in the fault zones on the measureable system responses such as pressure and temperature, and the most sensitive system responses among them. From the data-worth analysis, we determined the most valuable observation data to be measured for the best prediction of CO_2 distribution in the faults. These results can be used to guide field monitoring efforts to measure CO_2 saturation in order to calibrate and constrain active seismic monitoring used to characterize the extent and properties of fault zones relevant to EGS objectives.

The results of the forward simulations of 30 days of push and subsequent 30 days of pull revealed several interesting findings. First, injected CO_2 reached a higher depth in the conjugate fault than the main fault after the push. CO_2 was injected at Z between −3018 m and −3024 m, and reached $Z = -2070$ m and −1890 m in the main and conjugate faults, respectively. This was because the high-permeability zones of the country rock were concentrated around the conjugate fault allowing displaced water to leave the fault zone and CO_2 to flow upward in the fault zone. To quantify the effect of high-permeability zones in the system, we simulated the push-pull processes in a homogeneous reservoir without the high-permeability zones of country rock. This case showed that the CO_2 approached $Z = -2060$ m and −2040 m in the main and conjugate faults, respectively. The second main observation is that most of the injected CO_2flowed into the highly permeable fault gouge both in the main and conjugate faults during the push phase. In the following pull phase, some of the injected CO_2 was produced back through the fault slip plane and fault gouge, while significant amounts of CO_2 continued to flow upward through the damage zones by the buoyancy effect.

The results of the formal sensitivity analysis presented quantitatively the effects of unknown parameters of the fault zones on the system responses. The unknown

parameters included the absolute permeability, and the parameters of the relative permeability and capillary pressure functions in the fault slip plane, fault gouge, and damage zone. During the push phase, the most influential parameters were the capillary pressure parameters and irreducible saturations of gaseous and aqueous phases in the fault gouge, and irreducible saturation of gaseous phase in slip plane. During the pull phase, the most influential parameters were the irreducible saturation of gaseous phase and capillary pressure parameter in fault gouge, irreducible saturation of gaseous phase in slip plane, and irreducible saturations of gaseous phase and permeability in damage zone. During both push and pull phases, pressure observations were much more sensitive than temperature observations. However, temperature observation will hardly generate significant additional cost relative to the major cost which will occur in drilling wells rather than in monitoring systemresponse.

With the most influential parameters and output responses, we conducted a data-worth analysis in each of push and pull phases. The objective of the data-worth analysis was to minimize the prediction uncertainty of CO_2 distribution in the main and conjugate faults. The results of the data-worth analysis showed that the most valuable measurement data were the pressure of the main fault at $Z = -2520$ m and the pressure of the conjugate fault at $Z = -2100$ m in the push and pull phases, respectively.

We varied observation time and measurement uncertainty of pressure observation, in order to assess their impact on the data-worth analysis. Data observation time significantly affected the data worth and prediction uncertainty both in push and pull phases, while the effect of measurement uncertainty was not as significant. Once the allowable prediction uncertainty and expected measurement uncertainty are determined, we can decide the minimum monitoring time and the observation data to be measured for the best prediction of CO_2 distribution in the fault zones.

The purpose of data-worth analysis in this study was to minimize the prediction uncertainty of CO_2 distribution in the fault zones. The relative data worth of each measurement would change if the purpose of the data-worth analysis were the reduction of uncertainty in the estimation of unknown parameters. Still, the impact of the unknown parameters can be effectively managed in our proposed approach to reduce the prediction uncertainty because the prediction uncertainty arises from the unknown parameters.

Although this study was carried out in an idealized 2D model system, the approach we describe is applicable to any system and can be used to design monitoring approaches to collect the most valuable data. These data can then be used to make point measurements to calibrate and constrain active seismic, well logging, or other

monitoring data collected in campaigns aimed at better characterizing permeable faults and fractures critical for EGS. Our envisioned work flow includes active seismic monitoring at Dixie Valley coupled with the data on pressure, temperature, and saturation during the push-pull process.

Acknowledgements

This work was supported by the Office of Energy Efficiencyand Renewable Energy, Geothermal Technologies Office, U.S. Department of Energy, and additionally supported by the Assistant Secretary for Fossil Energy (DOE), Office of Coal and Power Systems, through the National Energy Technology Laboratory (NETL), by Lawrence Berkeley National Laboratory under Department of Energy Contract No. DE-AC02-05CH11231, and by EDRA. The authors appreciate Mr. Joe Iovenitti (consulting geoscientist and principal geologist) for providing the fine resolution imagesof cross sections of geological structure in Fig. 1.

References

Blackwell et al., 2007

D.D. Blackwell, R.P. Smith, M.C. Richards**Exploration and development at Dixie Valley, Nevada: summary of DOE studies**

Proceedings, 32nd Workshop of Geothermal Reservoir Engineering (2007), p. 16

View Record in Scopus

Blackwell et al., 2009

D.D. Blackwell, R.P. Smith, A. Waibel, M.C.Richards, P. Step**Why Basin and Range systems are hard to find II: structural model of the producing geothermal system in Dixie Valley, Nevada**

Geotherm. Resour. Counc. Trans., 33 (2009), pp. 441-446

Borgia et al., 2017

A. Borgia, C.M. Oldenburg, R. Zhang, L. Pan, T.M.Daley, S. Finsterle, T.S. Ramakrishnan**Simulations of CO_2 injection into fractures and faults for improving their geophysical characterization at EGS sites**

Geothermics, 69 (2017), pp. 189-201

ArticleDownload PDFView Record in Scopus

Corey, 1954

A.T. Corey**The interrelation between gas and oil relative permeabilities**

Producers Mon., 19 (1) (1954), pp. 38-41

View Record in Scopus

Finsterle and Zhang, 2011

S. Finsterle, Y. Zhang**Solving iTOUGH2 simulation and optimization problems using the PEST protocol**
Environ. Modell. Softw., 26 (7) (2011), pp. 959-968
ArticleDownload PDFView Record in Scopus

Finsterle, 1999

S. Finsterle**iTOUGH2 User's Guide**
Earth Science Division, Lawrence Berkeley National Laboratory(1999)

Finsterle, 2015

S. Finsterle**Practical notes on local data-worth analysis**
Water Resour. Res., 51 (12) (2015), pp. 9904-9924
CrossRefView Record in Scopus

Gudmundsson et al., 2002

A. Gudmundsson, I. Fjeldskaar, S.L. Brenner**Propagation pathways and fluid transport of hydrofractures in jointed and layered rocks in geothermal fields**
J. Volcanol. Geotherm. Res., 116 (3) (2002), pp. 257-278
ArticleDownload PDFView Record in Scopus

Iovenitti et al., 2013

J. Iovenitti, J. Sainsbury, I. Tibuleac, R. Karlin, P.Wannamaker, V. Maris, D. Blackwell, M. Thakur, F.H. Ibser, J.Lewicki, B.M. Kennedy**EGS exploration methodology project using the Dixie Valley geothermal system, Nevada**
Proceedings, 38th Workshop on Geothermal Reservoir Engineering Stanford University, Stanford, California (2013)

Iovenitti et al., 2016

J. Iovenitti, F.H. Ibser, M. Clyne, J. Sainsbury, O.Callahan**The basin and range Dixie Valley geothermal wellfield, Nevada, USA—a test bed for developing an enhanced geothermal system exploration favorability methodology**
Geothermics, 63 (2016), pp. 195-209
ArticleDownload PDF

Oldenburg et al., 2016

C.M. Oldenburg, T.M. Daley, A. Borgia, R. Zhang, C. Doughty, T.S. Ramakrishnan, B. Altundas, N. Chugunov**Preliminary simulations of carbon dioxide injection and geophysical monitoring to improve imaging and characterization of faults and fractures at EGS sites**
Proceedings, 41st Workshop on Geothermal Reservoir Engineering Stanford University, Stanford, California (2016)

Pan et al., 2015

L. Pan, N. Spycher, C. Doughty, K. Pruess**ECO2N V2. 0: A TOUGH2 Fluid Property Module for Mixtures of Water, NaCl, and CO_2**
Earth Science Division, Lawrence Berkeley National Laboratory(2015)

Pan, 2008

L. Pan**User Information for WinGridder Version 3.0**
Earth Science Division, Lawrence Berkeley National Laboratory(2008)

Smith_et_al._2011

R.P. Smith, R.P. Breckenridge, T.R. Wood**Preliminary Assessment of Geothermal Resource Potential at the UTTR**
Idaho National Laboratory (2011)

Steingrímsson, 2013

B. Steingrímsson**Geothermal well logging: temperature and pressure logs**
Tutorial-Geothermal Training Programme (2013)

Van Genuchten, 1980

M.T. Van Genuchten**A closed-form equation for predicting the hydraulic conductivity of unsaturated soils**
Soil Sci. Soc. Am. J., 44 (5) (1980), pp. 892-898
CrossRefView Record in Scopus

Wainwright and Finsterle, 2016

H.M. Wainwright, S. Finsterle**Global Sensitivity and Data-Worth Analyses in iTOUGH2**

Zhang et al., 201

R. Zhang, D. Vasco, T.M. Daley, W. Harbert**Characterization of a fracture zone using seismic attributes at the In Salah CO_2 storage project**
Interpretation, 3 (2) (2015), pp. SM37-SM46
CrossRefView Record in Scopus

3) By running forward simulations, evaluate the sensitivity coefficients, $\partial z_i / \partial p_j$ of all observations and predictions.

4) Evaluate the covariance matrix of the estimated parameters, C_{pp}, using the following equation.

$$C_{pp} = s_0^2 \left(J^T C_{zz}^{-1} J \right)^{-1} \tag{4}$$

where, s_0^2 is the estimated error variance, which is set to 1 in cases without actually measured data; J is the Jacobian matrix, which contains the sensitivity coefficients of $\partial z_i / \partial p_j$. C_{zz} is the covariance matrix of measurement errors and expected errors of predictions (σ_{z_i}), which has σ_{z_i} as its diagonal components.

1) Propagate the uncertainty of the estimated parameters,C_{pp}, to the uncertainty of predictions,

$$C_{\hat{z}\hat{z}} = \widehat{J} C_{pp} \widehat{J}^T \tag{5}$$

where, $\widehat{J}$ is the Jacobian matrix only involving sensitivity coefficients of the predictions.

1) Remove one actual observation datum labeled k and re-estimate the covariance matrix of parameter, $C_{pp,-k}$.

2) Re-evaluate the covariance matrix of the model predictions, $C_{\hat{z}\hat{z},-k}$.